

# Deglaciation drove seawater infiltration and slowed submarine groundwater discharge

Received: 4 March 2024

Accepted: 23 June 2025

Published online: 6 August 2025



S. ten Hietbrink<sup>1,2</sup>✉, H. Patton<sup>3</sup>, B. Dugan<sup>4,5</sup>, B. Szymczycha<sup>6</sup>, A. Sen<sup>7,8</sup>,  
A. Lepland<sup>9,10,11</sup>, J. Knies<sup>3,9</sup>, J.-H. Kim<sup>12</sup>, N.-C. Chen<sup>1,2</sup> & W.-L. Hong<sup>1,13</sup>✉

Submarine groundwater discharge—the flow of groundwater into the ocean—plays an important role in shaping coastal biogeochemical cycles. The absence of temporal constraints on offshore groundwater dynamics driven by proximal glacial loading hinders our assessment of how its circulation may vary in conceivable ice-free polar regions. Here we estimate residence times of saline groundwater at an active submarine groundwater discharge and methane seep site off the coast of northern Norway, near the continental shelf break. The subsurface hydrology in this area experienced drastic changes due to Fennoscandian Ice Sheet dynamics, offering insights into the consequences of glacial–interglacial transitions for offshore groundwater. Using radiocarbon dating of dissolved inorganic carbon in the upwards-advected groundwater, we determined saline groundwater residence times of 11.5 to 8.8 kyr and 4.8 to 2.6 kyr at two distinct discharge sites. The presence of a meteoric water component in sediment porewaters confirms offshore groundwater freshening driven by past glacial loading. This indicates that, as the ice sheet retreated and sea levels rose, seawater began to infiltrate the subsurface, replacing freshwater recharge. Our results provide observational evidence pinpointing the onset of seawater infiltration following deglaciation of the margin. These findings suggest that retreating marine-terminating glaciers will profoundly alter offshore groundwater composition and reduce discharge rates.

The inflow of groundwater through sediments into the marine environment—a process known as submarine groundwater discharge (SGD)—transports critical solutes such as nutrients<sup>1–6</sup>, dissolved carbon compounds<sup>7,8</sup> and trace metals<sup>9</sup> into the coastal ocean. Dedicated efforts to quantify the global importance of offshore groundwater circulation have demonstrated its pronounced influence on coastal biogeochemical cycles<sup>10–16</sup> and biological communities<sup>16–18</sup>. Regardless of the well-established implication on modern ocean biogeochemistry,

it is unclear whether the process was equally efficient in transporting solutes to the ocean in the past, for instance during glacial periods when the global water circulation was drastically different<sup>19,20</sup>.

Increased hydraulic head gradients introduced by ice sheet loading have been postulated to modify large-scale groundwater systems and flush entire groundwater aquifers<sup>21–26</sup>, resulting in offshore freshened groundwaters and potentially in the discharge of freshened fluids along continental margins. Furthermore, eustatic sea-level changes

<sup>1</sup>Department of Geological Sciences, Stockholm University, Stockholm, Sweden. <sup>2</sup>Bolin Centre for Climate Research, Stockholm University, Stockholm, Sweden. <sup>3</sup>C3: Centre for ice, Cryosphere, Carbon and Climate, UiT The Arctic University of Norway, Tromsø, Norway. <sup>4</sup>Department of Geophysics, Colorado School of Mines, Golden, CO, USA. <sup>5</sup>Hydrologic Science and Engineering Program, Colorado School of Mines, Golden, CO, USA. <sup>6</sup>Institute of Oceanology Polish Academy of Sciences, Sopot, Poland. <sup>7</sup>The University Centre in Svalbard, Longyearbyen, Norway. <sup>8</sup>Nord University, Bodø, Norway. <sup>9</sup>Geological Survey of Norway, Trondheim, Norway. <sup>10</sup>Department of Geology, University of Tartu, Tartu, Estonia. <sup>11</sup>Department of Geology, University of Technology, Tallinn, Estonia. <sup>12</sup>Marine Geology and Energy Division, Korea Institute of Geoscience and Mineral Resources, Daejeon, South Korea. <sup>13</sup>Baltic Sea Centre, Stockholm University, Stockholm, Sweden. ✉e-mail: [sophie.ten.hietbrink@geo.su.se](mailto:sophie.ten.hietbrink@geo.su.se); [wei-li.hong@geo.su.se](mailto:wei-li.hong@geo.su.se)

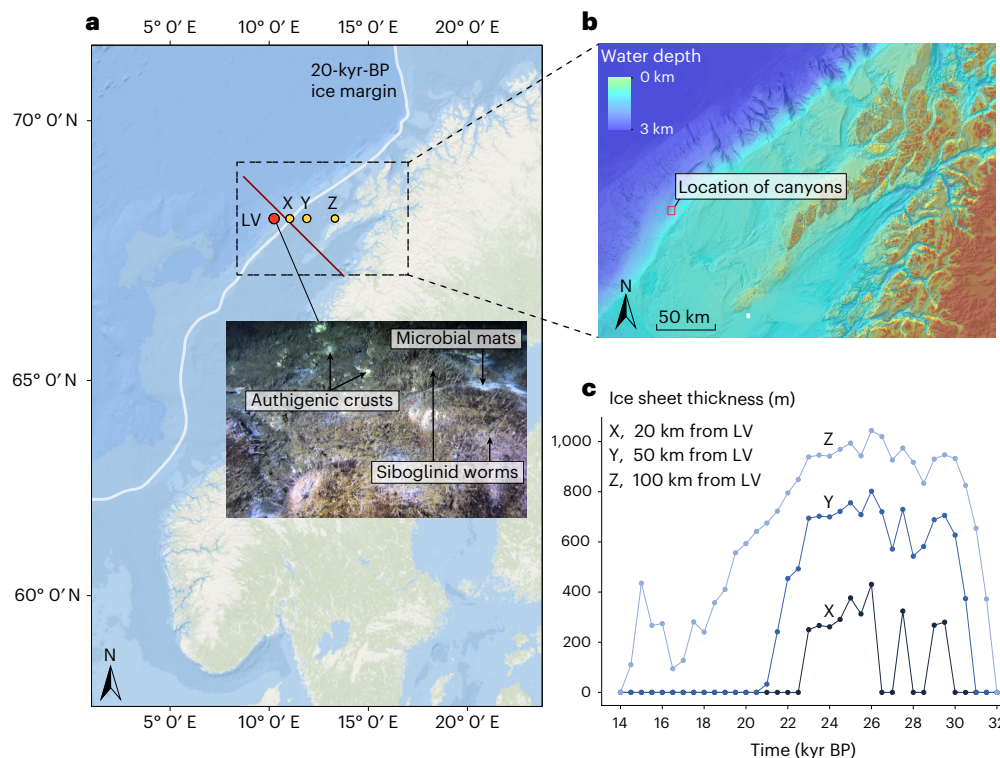


**Fig. 1 | Sample site location and ice sheet extent.** **a, b**, Cores were taken 80 km west of the Lofoten Archipelago offshore northern Norway at ca. 800 m water depth (**a**, with zoom in **b**). The sample site is indicated by the red dot with the label 'LV'. The yellow markers with labels 'X', 'Y' and 'Z' indicate the locations where ice sheet thickness data were extracted from a numerical model. The dark-red line indicates the position of the geological profile shown in Extended Data Fig. 1. The 20-kyr-BP ice margin extent was redrawn from ref. 45. Two canyons in the area are characterized by submarine groundwater discharge and cold seep features such as microbial mats, siboglinid worms and crusts of authigenic carbonate and

barite<sup>17,28</sup>. Push cores were obtained from two habitats: microbial mats (BacMat) and worm tuff (Worm). In addition, a background core (Background) upslope just outside of the discharge area was obtained. **c**, Ice sheet thickness between 32 and 14 kyr BP at three locations east of the LV site ('X', 'Y' and 'Z' from **a**). Basemap data in **b** from the GEBCO\_2024 Grid (<https://doi.org/10.5285/1c44ce99-0a0d-5f4f-e063-7086abc0ea0f>). Credit: basemap in **a**, Esri, Garmin, GEBCO, NOAA NGDC and other contributors (<https://www.arcgis.com/home/item.html?id=67ab7f7c535c4687b6518e6d2343e8a2>).

over glacial–interglacial timescales have been proposed to modulate the seawater–fresh water interface in offshore aquifers by exposing or flooding the continental shelf, resulting in freshening or seawater infiltration into the aquifers, respectively<sup>13,16</sup>. Despite the theoretically sound foundation of these hypotheses, essentially no observational constraints on the temporal scales of groundwater flow across continental shelves are available to test them. The lack of empirical data to validate numerical models has been highlighted as a pressing issue in multiple recent reviews<sup>1,16</sup>. This deficiency leaves fundamental questions unanswered regarding groundwater residence times, that is, the duration that water parcels take from entering (recharging) and exiting (discharging) an aquifer. Consequently, variations in solute fluxes into the coastal ocean following deglaciation of continental margins remain unknown. The lack of temporal constraints of offshore groundwater flows during glacial–interglacial transitions also hinders our ability to predict changes in the offshore discharge of critical solutes for a potentially ice-free polar region in the future. This matter becomes even more urgent given the observation of dynamic groundwater bodies beneath the Greenland and Antarctic ice sheets driven by glacial recharge and forcing<sup>21,27</sup>. Obtaining constraints from an environment that experienced rapid changes in the offshore groundwater system owing to glacial dynamics would thus offer valuable insights.

The submarine canyons along the Lofoten–Vesterålen (LV) continental shelf break offshore northern Norway (Fig. 1) represent such a location where active discharge of freshened groundwater is proposed to be associated with glacial dynamics<sup>28</sup>. Here, we determine the radiocarbon (<sup>14</sup>C) ages of dissolved inorganic carbon (DIC) in sediment

porewaters to estimate the residence time of the saline groundwater component. This allows us to better resolve the onset of aquifer salinization, disclosing the temporal evolution of the offshore groundwater system following the retreat of the Fennoscandian Ice Sheet (FIS) from the continental shelf.

## Porewater profiles attest to a preserved groundwater signal

Active groundwater discharge occurs in two submarine canyons on the continental shelf break of the LV margin<sup>28</sup> (Fig. 1 and Extended Data Fig. 1), providing an opportunity to investigate the groundwater composition of this offshore aquifer. Different DIC end-members in the porewater can clearly be differentiated using  $\delta^{13}\text{C}$  and the percent modern carbon (pMC). Below 5 cm sediment depth in cores PC29 and GS002PC01, including the sulfate–methane transition zone (SMTZ) in PC29, the DIC is depleted in <sup>14</sup>C (Fig. 2). In PC29, DIC originating from the anaerobic oxidation of methane (AOM) has the lowest  $\delta^{13}\text{C}$  value of  $-49.4\text{‰}$  and shows an additional <sup>14</sup>C depletion of 12 pMC (Fig. 2c). Porewater impacted by seawater is near modern, with pMC values of  $>97\%$ . Reaction-transport modelling of <sup>14</sup>C<sub>DIC</sub> profiles yielded an upwards groundwater advection velocity of approximately  $0.1\text{ m yr}^{-1}$  (Extended Data Fig. 2). This corresponds with previously derived velocities from other solute profiles<sup>28</sup>. The upwards movement of groundwater is further supported by concentration gradients of dissolved barium, boron and lithium<sup>28</sup> (Extended Data Fig. 3). This indicates a well-preserved groundwater source signal in the sampled porewaters. The notable advection velocities help reduce the reaction

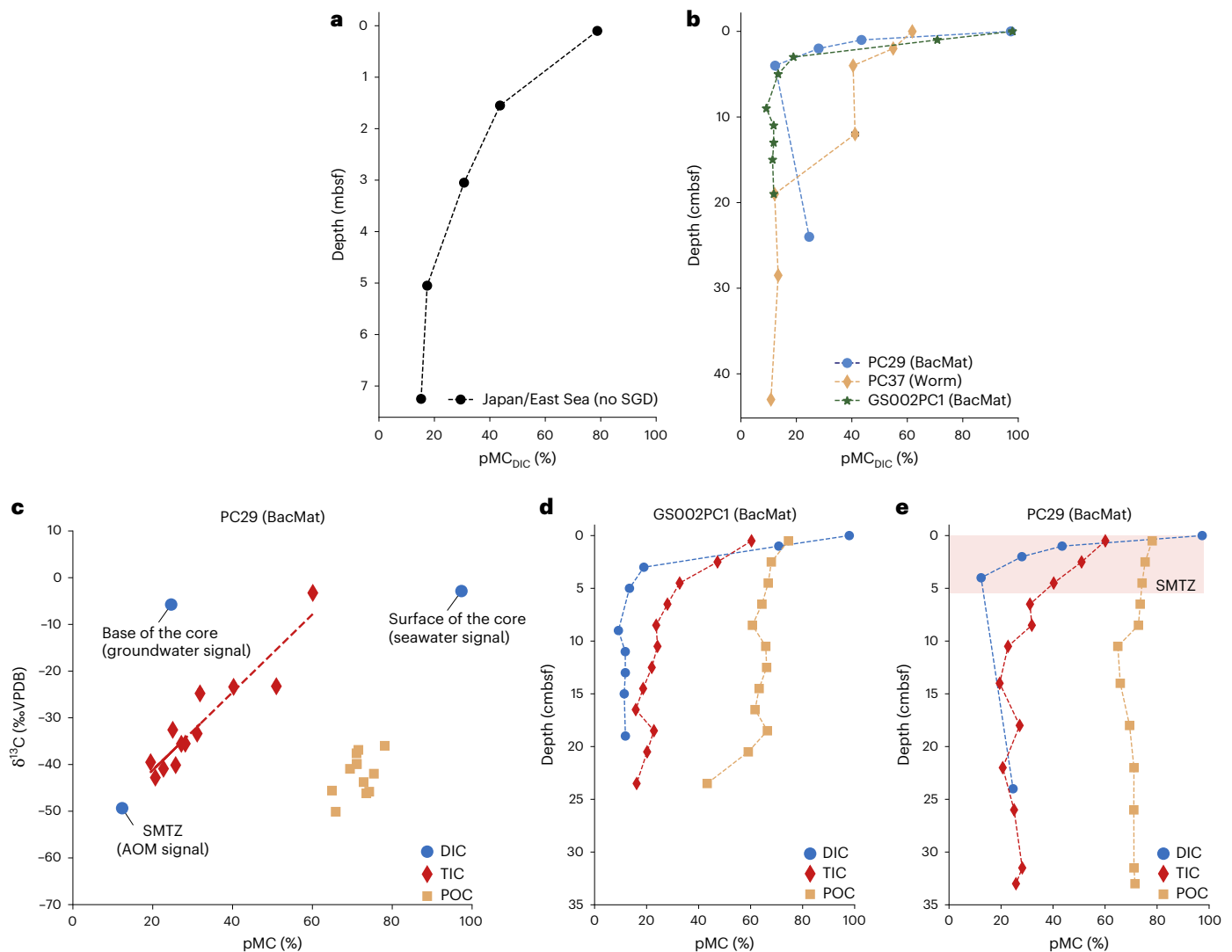


**Fig. 2 | Downcore radiocarbon profiles.** **a**, The DIC radiocarbon content in percent modern carbon (pMC) of a 7-m-long core taken at a site in the Japan/East Sea unaffected by SGD is dominantly governed by radioactive decay after sediment burial. **b**, At the LV site with active SGD, radiocarbon-depleted DIC is found much closer to the sediment–seawater interface at a depth of ~5 cm below seafloor (cmbsf) as a result of upwards advection. **c**, Three DIC end-members can

be identified in the porewater: groundwater-influenced porewater, seawater-influenced porewater and AOM-influenced porewater. Authigenic carbonate precipitation is represented by the linear correlation of TIC. **d,e**, Downcore radiocarbon content of DIC, TIC and POC for cores GS002PC1 (**d**) and PC29 (**e**). mbsf, metres below seafloor.

time of groundwater during subsurface transit, thereby preserving the original <sup>14</sup>C content.

## Evidence of offshore groundwater freshening and carbon cycling

Sediment profiles from the SGD area display a decrease in porewater salinity, with chlorinity values lower than that of seawater (Fig. 3). Chlorinities below 500 mM were measured, corresponding with a decrease of >10% compared with a 560 mM seawater chlorinity. Additionally, δ<sup>2</sup>H<sub>H<sub>2</sub>O</sub> and δ<sup>18</sup>O<sub>H<sub>2</sub>O</sub> values are lower than that of seawater and plot close to the local meteoric water line of Lista, southern Norway (Fig. 3), suggesting a groundwater component sourced from precipitation<sup>29,30</sup>. Maximum δ<sup>2</sup>H and δ<sup>18</sup>O differences of 11.7‰ and 2.0‰, respectively, were found from porewater influenced by bottom seawater. These variations exceed the spatial and temporal variations typically observed in the stable water isotopic composition of seawater<sup>28,31,32</sup>. There is no strong indication that the source aquifer in the Cenozoic strata (Extended Data Fig. 1) is fully freshened at present; instead, brackish conditions seem to predominate. Surprisingly, the background core

(PC23) also shows downcore freshening (Fig. 3). This might indicate that offshore freshening is not merely confined to the in-depth studied SGD area displaying seafloor biological activity and may be more widespread than initially assumed<sup>28</sup>.

Evident methane-derived authigenic carbonate imprints were observed in the isotopic signatures of the inorganic particulate fraction of the sediment, here referred to as total inorganic carbon (TIC) (Fig. 2c and Extended Data Fig. 4). In the background core, average δ<sup>13</sup>C<sub>TIC</sub> values of 0.32 ± 0.85‰ (1σ) and δ<sup>18</sup>O<sub>TIC</sub> of -3.79 ± 3.02‰ (1σ) were measured. For the cores sampled from the SGD sites, δ<sup>13</sup>C<sub>TIC</sub> values as low as -58.0‰ and δ<sup>18</sup>O<sub>TIC</sub> values as high as 4.0‰ were found (Extended Data Fig. 4). These low δ<sup>13</sup>C<sub>TIC</sub> values are a direct consequence of the sequestration of <sup>13</sup>C-depleted methane into the marine sediment<sup>33–36</sup>. A similar depletion is observed in the <sup>14</sup>C content of TIC. When the authigenic component becomes progressively more dominant than the biogenic carbonate, emulated by a lower δ<sup>13</sup>C<sub>TIC</sub>, the TIC shifts towards the <sup>14</sup>C signatures of DIC. This manifests in a linear relation between the <sup>13</sup>C and <sup>14</sup>C isotopic signatures of TIC<sup>37</sup> (Fig. 2c) and partially explains the <sup>14</sup>C offset with the particulate

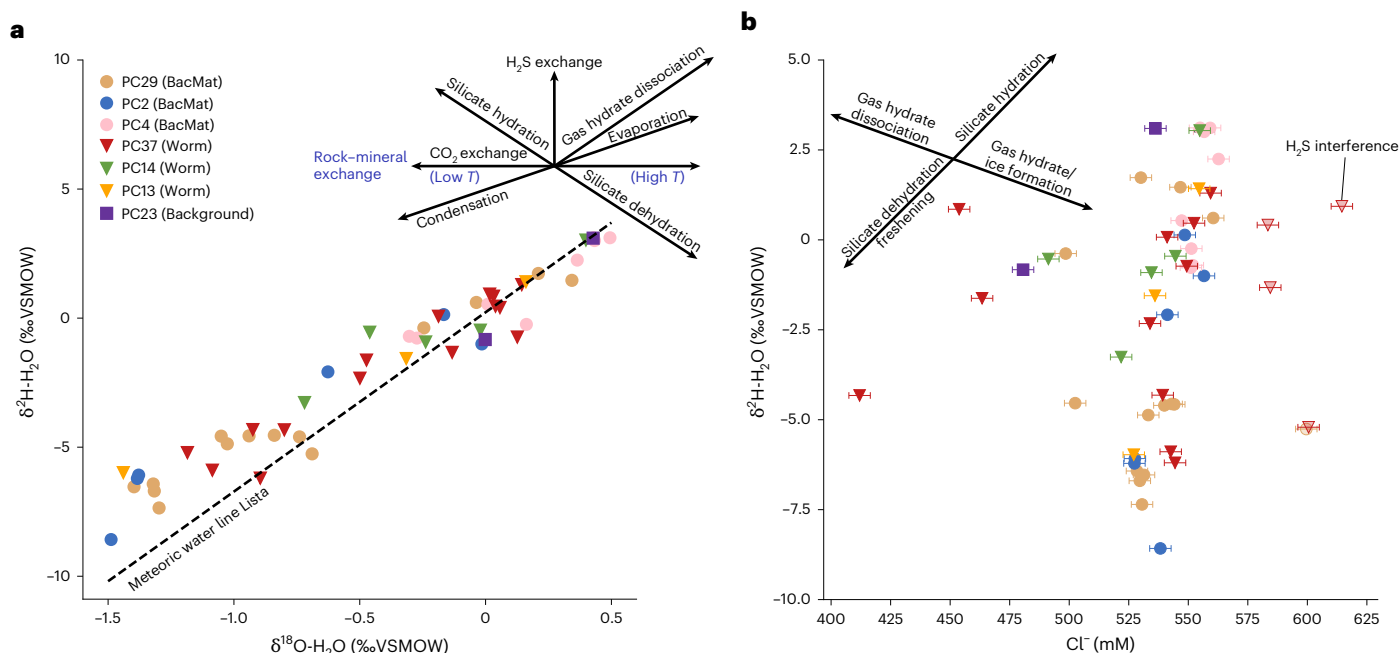


**Fig. 3 | Meteoric water influences in the porewater. a**, Meteoric water influences are confirmed by stable isotopes of water plotting near the local meteoric water line<sup>29,30</sup> ( $\delta^2\text{H} = 6.95 \delta^{18}\text{O} + 0.23$ ) of Lista (located in southern Norway) and a chlorinity lower than seawater. **b**, The chlorinities above the seawater level

of 560 mM, indicated with the partially transparent symbols, are probably an artefact from  $\text{H}_2\text{S}$  interference during titration. The  $\text{Cl}^-$  error bar in **b** represents the s.d. of the seawater standards ( $n = 43$ ).

organic carbon fraction of the sediment (POC). The increase in  $\delta^{18}\text{O}_{\text{TIC}}$  from the background core can be explained by the equilibrium with seawater (Extended Data Fig. 5) and is within the range expected from ambient temperatures<sup>33</sup>.

### <sup>14</sup>C content shows that DIC and $\text{CH}_4$ have ex situ sources

Because DIC has the lowest  $^{14}\text{C}$  content among the different carbon pools at the core base and exhibits relatively stable profiles below 5 cmbsf (Fig. 2d), we can conclude that the DIC must originate from an external carbon source not associated with in situ (that is, within the recovered sediments) organic matter degradation or carbonate dissolution. This aligns with our anticipated outcome, as DIC is transported into the marine sediment through the upwards movement of groundwater. We also record an abrupt change in the  $^{14}\text{C}_{\text{DIC}}$  signal in the top 5 cm of the sediment, corresponding with the SMTZ (Fig. 2e; Extended Data Fig. 6). Here, DIC is actively produced through AOM. By comparing the stable and  $^{14}\text{C}$  isotopic signatures of DIC (Fig. 2c), we find that the introduction of carbon from assumed  $^{14}\text{C}$ -free methane oxidation results in the  $^{14}\text{C}$  dilution of DIC. This yields the 12-pMC negative offset from the porewater at the core base (Fig. 2c). To validate this  $^{14}\text{C}$  dilution effect from AOM, we conducted sensitivity tests using varying methane  $^{14}\text{C}$  content in our reaction–transport model (Extended Data Fig. 7). The model results confirm that the methane has to be nearly  $^{14}\text{C}$ -free, consistent with the global compilation of methane  $^{14}\text{C}$  ages<sup>38</sup>, and therefore probably originates from much deeper depths than our recovered sediments. However, more importantly, the  $^{14}\text{C}$  alterations induced by AOM necessitate the use of DIC from below the SMTZ to accurately infer the age of groundwater via  $^{14}\text{C}$  dating.

During groundwater flow within the rock aquifer, additional  $^{14}\text{C}$ -depleted carbon may be introduced through ex situ carbonate dissolution and the degradation of organic matter, potentially leading to overestimated residence times (see the Supplementary Information for detailed discussion). On the basis of the relatively high  $\delta^{13}\text{C}_{\text{DIC}}$  values and the somewhat elevated  $\text{Ca}^{2+}$  concentrations compared with that of seawater (Extended Data Fig. 3), the excess DIC,

that is, the surplus of what would be expected from a seawater and fresh water mixture, is probably a result of carbonate dissolution. This possibility was addressed by including a term for chemical reactions within the mixing model in equation (2) used for the calculation of the saline groundwater residence time, where excess DIC was attributed to aquifer biogeochemical reactions or carbonate dissolution that add  $^{14}\text{C}$ -depleted carbon. All anticipated DIC sources within the rock aquifer, including carbonates, organic matter, methane and fresh palaeogroundwater, are expected to be low in radiocarbon, prompting us to propose that seawater infiltration into the offshore aquifer following ice sheet regression could have introduced the relatively  $^{14}\text{C}$ -enriched DIC.

### Seawater infiltration followed the retreat of the FIS

On the basis of the porewater composition (Fig. 3), we argue that the discharged groundwater consists of two main components: fresh submarine groundwater of meteoric origin (fSG), and a seawater submarine groundwater component (sSG). To separate these two components, chlorinity end-member values of 0 mM for fSG and 560 mM for sSG were used. The groundwater residence time of sSG can be derived from the degree of  $^{14}\text{C}$  decay and a mixing model that accounts for fSG, sSG and chemical reactions (see Methods for detailed calculation). To convert  $^{14}\text{C}$  decay into a groundwater residence time, the initial  $^{14}\text{C}_{\text{DIC}}$  content of the fSG and sSG groundwater components directly after recharge ( $A(t_0)$ ) should be estimated. The initial subglacial water  $^{14}\text{C}_{\text{DIC}}$  content ( $A_{\text{fSG}}(t_0)$ ) is influenced by various factors, including the equilibration time with atmospheric  $\text{CO}_2$ , the incorporation of old ice and the microbial activity at the base of the ice sheet. As a result, subglacial waters generally show lower  $^{14}\text{C}_{\text{DIC}}$  contents than supraglacial water<sup>39,40</sup>. On the basis of a study conducted at the Greenland Ice Sheet<sup>40</sup>,  $A_{\text{fSG}}(t_0)$  is estimated to average around  $80 \pm 5$  pMC. The initial marine  $^{14}\text{C}_{\text{DIC}}$  content ( $A_{\text{sSG}}(t_0)$ ) is presumed to be 98 pMC, on the basis of the contemporary bottom seawater  $^{14}\text{C}_{\text{DIC}}$  content (Fig. 2), factoring in the local marine reservoir effect. To address potential variations in initial  $^{14}\text{C}_{\text{DIC}}$  activities, an uncertainty analysis was conducted by



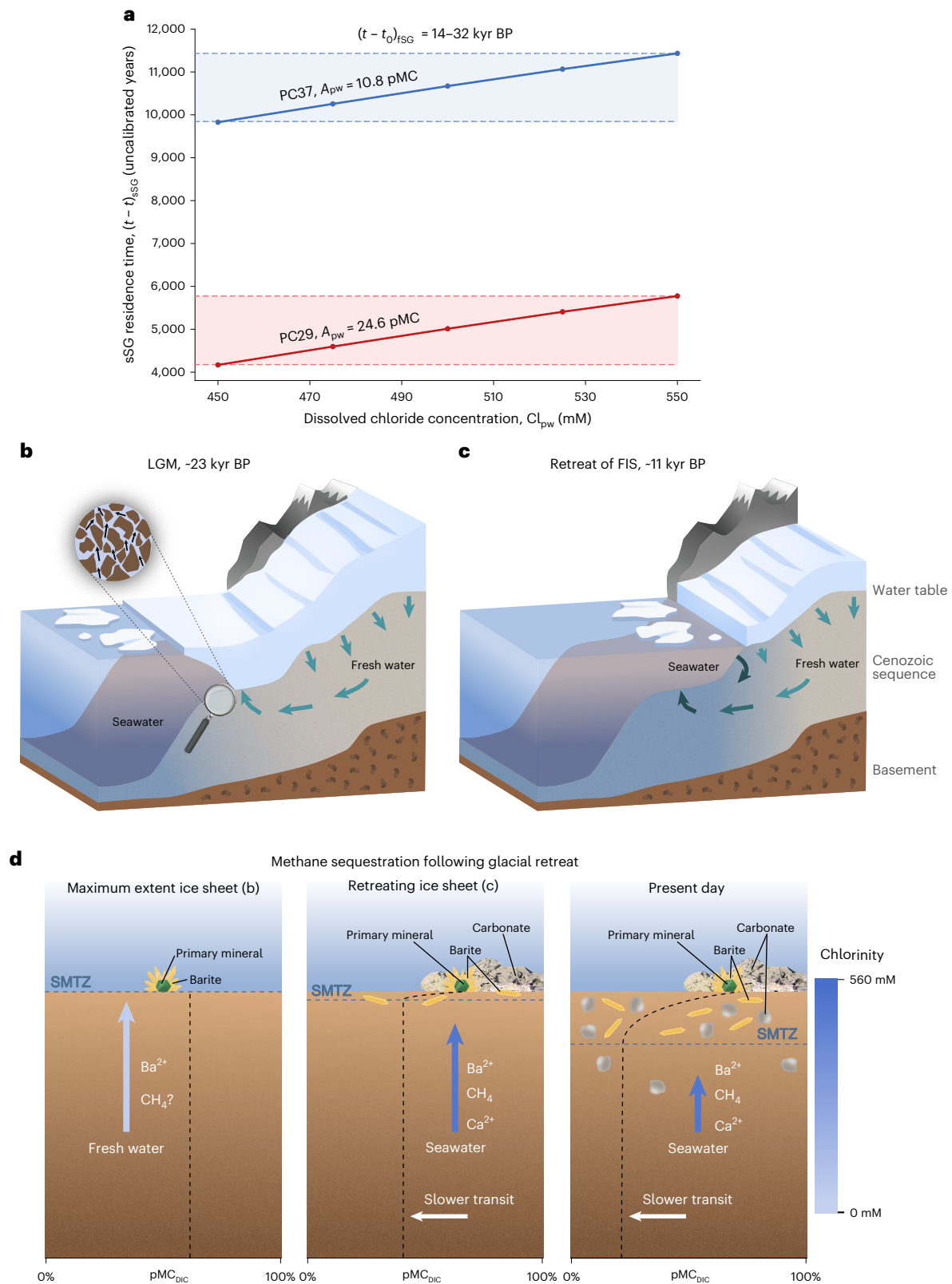


**Fig. 4 | Groundwater residence times of the sSG and a conceptual depiction of the proposed changes in offshore subsurface hydrology and sediment geochemistry following the retreat of the FIS. a**, sSG groundwater residence times for a chlorinity range of 450–550 mM, indicated by the error range, based on the  $^{14}\text{C}_{\text{DIC}}$  content of porewater from the core base of PC29 and PC37. **b,c**, Meteoric water imprints in marine sediment porewaters indicate a history of offshore aquifer freshening, attributed to increased hydraulic head gradients

as a result of glacial loading during the Last Glacial Maximum (**b**) while saline groundwater residence times illustrate that, after the collapse of the FIS and retreat of marine-based outlet glaciers, seawater started infiltrating the offshore aquifer (**c**). **d**, Decelerating groundwater discharge velocities due to glacial unloading allowed the SMTZ to move into the sediments, resulting in the formation of barite and carbonate within the sediments opposed to on the seafloor. Figure created with Affinity Designer.

lowering the  $A_{\text{fsg}}(t_0)$  and  $A_{\text{ssg}}(t_0)$  values to simulate the addition of  $^{14}\text{C}$ -depleted carbon (Extended Data Fig. 8). This analysis revealed an uncertainty range of approximately 1,600 years in the age estimates presented in this study (Fig. 4a) for different  $A_{\text{ssg}}(t_0)$  values, while variations in  $A_{\text{fsg}}(t_0)$  values contributed negligible uncertainty.

Without the presence of the FIS and its extensive subglacial drainage network<sup>41,42</sup>, conditions do not allow for the recharge of fresh groundwater into the continental margin, which would explain the observed offshore freshening. This constrains the timing of meteoric groundwater recharge, given by  $(t - t_0)_{\text{fsg}}$ , which is needed to calculate the saline groundwater residence time using equation (8). Relative sea-level fluctuations during the last deglaciation period in the LV region are predominantly influenced by glacial isostatic rebound and are not well constrained<sup>43</sup>. The limited data available indicate that, around 16.0 kyr before 1950 (BP), relative sea levels were 60 m or lower, and dropped to approximately –15 m during the Younger Dryas period (–14.0–11.7 kyr BP)<sup>43</sup>. Following the Younger Dryas, there was a transgressive phase until 6.0 kyr BP when relative sea levels reached 5 m (ref. 43). These sea-level variations are comparatively minor in scale when juxtaposed with changes in ice sheet thickness (Fig. 1c). Therefore, the primary driving force behind freshwater recharge on the LV continental shelf is attributed to ice sheet extent and thickness. Modelling of the FIS suggests that grounded ice extended beyond the Lofoten Islands to the continental slope between 32 and 14 kyr BP, reaching a local maximum extent and volume between 26 and 23 kyr BP<sup>42,44</sup> during the Last Glacial Maximum (Fig. 1c). This chronology is consistent with a recent empirically based time slice reconstruction of the Eurasian ice sheet deglaciation<sup>45</sup>. During this maximum extent, the modelled grounding line of the ice sheet was <20 km from the current LV site (Fig. 1). To be on the conservative side, a time constraint  $((t - t_0)_{\text{fsg}})$  of 32 to 14 kyr BP was used for fSG recharge (Fig. 4a and Extended Data Fig. 8).

We used the porewater  $^{14}\text{C}_{\text{DIC}}$  content from the bottom of cores PC37 and PC29 (Fig. 2b) to calculate sSG residence times, as alkalinity data needed to estimate DIC excess were available for these two cores. Alkalinity data are not available for GS002PC1, hence it was excluded from the calculations. Nevertheless, GS002PC1 exhibits  $^{14}\text{C}_{\text{DIC}}$  contents very similar to those of PC37 (Fig. 2b), suggesting that its sSG residence times are likely comparable. The sSG residence times were calculated for chlorinity contents of 450, 475, 500, 525 and 550 mM, corresponding to seawater fractions ( $f_{\text{ssg}}$ ) of 0.804, 0.848, 0.893, 0.938 and 0.982, respectively (Fig. 4a). This range encompasses the majority of the porewater chlorinities (Fig. 3b). Calibration with the IntCal20 curve<sup>46</sup> yielded sSG residence times of 11,546 to 8,844 yr ( $2\sigma$ ) for PC37 and 4,784 to 2,576 yr ( $2\sigma$ ) for PC29. This means that the saline groundwater with the longest residence time was recharged between 11,546 and 8,844 yr BP, corresponding with the period of rapid FIS retreat and sea-level transgression that followed the Younger Dryas stadial<sup>42,45</sup>. It is plausible that seawater began infiltrating the continental margin as early as 16 kyr BP, when the FIS started retreating from the continental shelf<sup>42,45,47</sup>. However, this groundwater would have discharged before the time of sampling, precluding definitive inferences. The residence time for PC29 is much shorter, although it remains difficult to conclude from the  $\text{pMC}_{\text{DIC}}$  profile that this data point accurately reflects the groundwater's  $^{14}\text{C}$  content (Fig. 2b). The observed variation between PC29 and PC37 can, at least in part, be attributed to differing flow paths and varying mixing with other groundwater bodies. The sSG residence times suggest that seawater infiltration continued for up to ~5,000 years or more after the retreat of the FIS from the continental shelf and coinciding sea-level rise<sup>42,45,47</sup>. Following sea-level rise, the infiltrated seawater probably mixed with the pre-existing fresh water in the aquifer, which had been displaced before glacial loading (Fig. 4c and Supplementary Information). This process resulted in the brackish signatures observed today. The porewater cation concentrations (Extended Data Fig. 3) can be attributed to alterations of an underlying

mafic body<sup>48</sup> that is located at a depth of approximately 1 km (ref. 28). This underscores that the observed flushing of this offshore aquifer is not merely confined to superficial layers but extends to substantial depths reaching up to 1 km.

## Authigenic precipitates as archives of discharge velocities

The authigenic minerals composed of Ca-carbonate and barite act as a geological archive of the depths of the SMTZ<sup>33,49</sup>. The barite is forged when groundwater rich in  $\text{Ba}^{2+}$  encounters sulfate-rich seawater, thereby recording the depth of sulfate penetration into the sediment<sup>49</sup>. The presence of barite on the seafloor suggests that the SMTZ once reached up to the sediment–water interface<sup>34</sup> (Fig. 4d). This is further evidenced by variably enriched  $^{34}\text{S}$  in barite crusts, indicating that the fluctuating SMTZ must have extended nearly to the seafloor<sup>34</sup>. Reaction–transport model experiments reveal that the vertical migration of the SMTZ throughout the sediment is to a large extent controlled by groundwater advection velocities<sup>50</sup> (Extended Data Fig. 9). To bring the SMTZ with current AOM rates to the sediment–water interface, upwards advection velocities on the order of  $1\text{ m yr}^{-1}$  or higher are required (Extended Data Fig. 9). Thus, solute fluxes were probably higher during periods of glaciation as a result of glacial loading and subsequent intensified hydraulic head gradients. The barite present within the shallow subsurface marine sediment at the LV site (Extended Data Fig. 10) marks the downwards movement of the SMTZ, reflecting the loss of hydraulic potential following the last deglaciation starting at ~22 kyr BP. Therefore, the distribution of barite within surface and subsurface sediments supports our conclusion from  $^{14}\text{C}_{\text{DIC}}$  ages that groundwater discharge weakened after the retreat of the FIS.

## Carbon sequestration accompanied seawater infiltration

SGD at high fluid advection velocities results in high methane fluxes to the overlying bottom ocean, thereby bypassing the benthic methane filter<sup>50–52</sup>, as confirmed by our numerical modelling (Extended Data Fig. 9). Sulfate-induced AOM may have been limited by the availability of sulfate in porewaters, as upwards groundwater advection probably prevented seawater from entering the sediments (Fig. 4d). On the other hand, the waning of SGD velocities during glacial retreat boosted sulfate supply in the shallow subsurface and the associated AOM. Together with the additional  $\text{Ca}^{2+}$  from aquifer salinization (Extended Data Fig. 3), a substantial portion of methane carbon was sequestered as authigenic carbonate (Fig. 4d). This interpretation is corroborated by the majority of previously reported U–Th ages of seafloor carbonate<sup>28</sup>, which coincide with the retreat of the FIS and the timing of seawater infiltration as observed in this study.

Our findings reveal a critical transition in subsurface hydrological dynamics as the FIS retreated from the LV continental margin and sea levels rose. This shift marked the replacement of offshore freshening, driven by glacial loading, with seawater-driven aquifer flushing. Authigenic mineral precipitates provide further evidence that this transition was accompanied by a deceleration in SGD velocities as hydraulic head gradients subsided. The deceleration of groundwater flow resulted in the present-day discharge of groundwater originating from the last deglaciation. It also enhanced carbon sequestration through methane oxidation and authigenic carbonate formation, facilitated by increased sulfate availability in marine sediments.

## Online content

Any methods, additional references, Nature Portfolio reporting summaries, source data, extended data, supplementary information, acknowledgements, peer review information; details of author contributions and competing interests; and statements of data and code availability are available at <https://doi.org/10.1038/s41561-025-01750-z>.

## References

- Santos, I. R. et al. Submarine groundwater discharge impacts on coastal nutrient biogeochemistry. *Nat. Rev. Earth Environ.* **2**, 307–323 (2021).
- Rodellas, V., Garcia-Orellana, J., Masqué, P., Feldman, M. & Weinstein, Y. Submarine groundwater discharge as a major source of nutrients to the Mediterranean Sea. *Proc. Natl Acad. Sci. USA* **112**, 3926–3930 (2015).
- Szymczycha, B., Vogler, S. & Pempkowiak, J. Nutrient fluxes via submarine groundwater discharge to the Bay of Puck, southern Baltic Sea. *Sci. Total Environ.* **438**, 86–93 (2012).
- Waska, H. & Kim, G. Submarine groundwater discharge (SGD) as a main nutrient source for benthic and water-column primary production in a large intertidal environment of the Yellow Sea. *J. Sea Res.* **65**, 103–113 (2011).
- Slopp, C. P. & Van Cappellen, P. Nutrient inputs to the coastal ocean through submarine groundwater discharge: controls and potential impact. *J. Hydrol.* **295**, 64–86 (2004).
- Rahman, S., Tamborski, J. J., Charette, M. A. & Cochran, J. K. Dissolved silica in the subterranean estuary and the impact of submarine groundwater discharge on the global marine silica budget. *Mar. Chem.* **208**, 29–42 (2019).
- Moore, W. S., Blanton, J. O. & Joye, S. B. Estimates of flushing times, submarine groundwater discharge, and nutrient fluxes to Okatee Estuary, South Carolina. *J. Geophys. Res. Oceans* **111**, C09006 (2006).
- Connolly, C. T., Cardenas, M. B., Burkart, G. A., Spencer, R. G. & McClelland, J. W. Groundwater as a major source of dissolved organic matter to Arctic coastal waters. *Nat. Commun.* **11**, 1479 (2020).
- Mayfield, K. K. et al. Groundwater discharge impacts marine isotope budgets of Li, Mg, Ca, Sr, and Ba. *Nat. Commun.* **12**, 148 (2021).
- Taniguchi, M., Burnett, W. C., Cable, J. E. & Turner, J. V. Investigation of submarine groundwater discharge. *Hydrol. Process.* **16**, 2115–2129 (2002).
- Moore, W. S. The subterranean estuary: a reaction zone of ground water and sea water. *Mar. Chem.* **65**, 111–125 (1999).
- Moore, W. S. The effect of submarine groundwater discharge on the ocean. *Annu. Rev. Mar. Sci.* **2**, 59–88 (2010).
- Post, V. E. et al. Offshore fresh groundwater reserves as a global phenomenon. *Nature* **504**, 71–78 (2013).
- Arévalo-Martínez, D. L. et al. Ideas and perspectives: land–ocean connectivity through groundwater. *Biogeosciences* **20**, 647–662 (2023).
- Lecher, A. L. Groundwater discharge in the Arctic: a review of studies and implications for biogeochemistry. *Hydrology* **4**, 41 (2017).
- Micallef, A. et al. Offshore freshened groundwater in continental margins. *Rev. Geophys.* **59**, e2020RG000706 (2021).
- Sen, A. et al. Atypical biological features of a new cold seep site on the Lofoten–Vesterålen continental margin (northern Norway). *Sci. Rep.* **9**, 1762 (2019).
- Luijendijk, E., Gleeson, T. & Moosdorf, N. Fresh groundwater discharge insignificant for the world's oceans but important for coastal ecosystems. *Nat. Commun.* **11**, 1260 (2020).
- Murakami, S., Ohgaito, R., Abe-Ouchi, A., Crucifix, M. & Otto-Bliesner, B. L. Global-scale energy and freshwater balance in glacial climate: a comparison of three PMIP2 LGM simulations. *J. Clim.* **21**, 5008–5033 (2008).
- Clark, P. U. & Mix, A. C. Ice sheets and sea level of the Last Glacial Maximum. *Quat. Sci. Rev.* **21**, 1–7 (2002).
- Liljedahl, L. C. et al. Rapid and sensitive response of Greenland's groundwater system to ice sheet change. *Nat. Geosci.* **14**, 751–755 (2021).
- Boulton, G. S. et al. Deep circulation of groundwater in overpressured subglacial aquifers and its geological consequences. *Quat. Sci. Rev.* **12**, 739–745 (1993).
- DeFoor, W. et al. Ice sheet–derived submarine groundwater discharge on Greenland's continental shelf. *Water Resour. Res.* **47**, 7 (2011).
- Person, M., McIntosh, J., Bense, V. & Remenda, V. H. Pleistocene hydrology of North America: the role of ice sheets in reorganizing groundwater flow systems. *Rev. Geophys.* **45**, RG3007 (2007).
- Siegel, J. et al. Influence of late Pleistocene glaciations on the hydrogeology of the continental shelf offshore Massachusetts, USA. *Geochim. Geophys. Geosyst.* **15**, 4651–4670 (2014).
- Clementi, V. J., Rosenthal, Y. & Bova, S. C. Deep submarine infiltration of altered geothermal groundwater on the south Chilean Margin. *Commun. Earth Environ.* **3**, 218 (2022).
- Gustafson, C. D. et al. A dynamic saline groundwater system mapped beneath an Antarctic ice stream. *Science* **376**, 640–644 (2022).
- Hong, W. L. et al. Discharge of meteoric water in the eastern Norwegian Sea since the last glacial period. *Geophys. Res. Lett.* **46**, 8194–8204 (2019).
- Jasechko, S. Global isotope hydrogeology—review. *Rev. Geophys.* **57**, 835–965 (2019).
- D'amore, F. & Panichi, C. Geochemistry in geothermal exploration. *Int. J. Energy Res.* **9**, 277–298 (1985).
- Voelker, A. H., Colman, A., Olack, G., Wanek, J. J. & Hodell, D. Oxygen and hydrogen isotope signatures of Northeast Atlantic water masses. *Deep Sea Res. Part II* **116**, 89–106 (2015).
- Schrag, D. P. et al. The oxygen isotopic composition of seawater during the Last Glacial Maximum. *Quat. Sci. Rev.* **21**, 331–342 (2002).
- Naehr, T. H. et al. Authigenic carbonate formation at hydrocarbon seeps in continental margin sediments: a comparative study. *Deep Sea Res.* **54**, 1268–1291 (2007).
- Wood, R. S., Lepland, A., Oglione, R. C., Houghton, J. & Fike, D. A. Microscale  $\delta^{34}\text{S}$  heterogeneities in cold seep barite record variable methane flux off the Lofoten–Vesterålen Continental Margin, Norway. *Earth Planet. Sci. Lett.* **574**, 117164 (2021).
- Bohrmann, G., Greinert, J., Suess, E. & Torres, M. Authigenic carbonates from the Cascadia subduction zone and their relation to gas hydrate stability. *Geology* **26**, 647–650 (1998).
- Greinert, J., Bohrmann, G. & Suess, E. Gas hydrate-associated carbonates and methane-venting at Hydrate Ridge: classification, distribution and origin of authigenic lithologies. *Geophys. Monogr.* **124**, 99–114 (2001).
- Logvina, E. A. et al. Correction of the measured radiocarbon age of carbonates from the discharge sites of hydrocarbon fluids. *Geochim. Int.* **50**, 1064–1069 (2012).
- Pohlman, J. W. et al. Methane sources in gas hydrate-bearing cold seeps: evidence from radiocarbon and stable isotopes. *Mar. Chem.* **115**, 102–109 (2009).
- Pain, A. J., Martin, J. B., Martin, E. E., Rennermalm, Å. K. & Rahman, S. Heterogeneous  $\text{CO}_2$  and  $\text{CH}_4$  content of glacial meltwater from the Greenland ice sheet and implications for subglacial carbon processes. *Cryosphere* **15**, 1627–1644 (2021).
- Andrews, M. G., Jacobson, A. D., Osburn, M. R. & Flynn, T. M. Dissolved carbon dynamics in meltwaters from the Russell Glacier, Greenland Ice Sheet. *J. Geophys. Res. Biogeosci.* **123**, 2922–2940 (2018).
- Shackleton, C. et al. Distinct modes of meltwater drainage and landform development beneath the last Barents Sea ice sheet. *Front. Earth Sci.* **11**, 1111396 (2023).
- Patton, H. et al. Deglaciation of the Eurasian ice sheet complex. *Quat. Sci. Rev.* **169**, 148–172 (2017).

43. Creel, R. C. et al. Postglacial relative sea level change in Norway. *Quat. Sci. Rev.* **282**, 107422 (2022).
44. Patton, H., Hubbard, A., Andreassen, K., Winsborrow, M. & Stroeve, A. P. The build-up, configuration, and dynamical sensitivity of the Eurasian ice-sheet complex to Late Weichselian climatic and oceanic forcing. *Quat. Sci. Rev.* **153**, 97–121 (2016).
45. Sejrup, H. P. et al. The role of ocean and atmospheric dynamics in the marine-based collapse of the last Eurasian Ice Sheet. *Commun. Earth Environ.* **3**, 119 (2022).
46. Reimer, P. J. et al. The IntCal20 Northern Hemisphere radiocarbon age calibration curve (0–55 cal kBP). *Radiocarbon* **62**, 725–757 (2020).
47. Stroeve, A. P. et al. Deglaciation of Fennoscandia. *Quat. Sci. Rev.* **147**, 91–121 (2016).
48. Lawrence, J. R., Gieskes, J. M. & Broecker, W. S. Oxygen isotope and cation composition of DSDP pore waters and the alteration of Layer II basalts. *Earth Planet. Sci. Lett.* **27**, 1–10 (1975).
49. Dickens, G. R. Sulfate profiles and barium fronts in sediment on the Blake Ridge: present and past methane fluxes through a large gas hydrate reservoir. *Geochim. Cosmochim. Acta* **65**, 529–543 (2001).
50. Sauer, S. et al. Methane transport and sources in an Arctic deep-water cold seep offshore NW Svalbard (Vestnesa Ridge, 79°N). *Deep Sea Res. Part I: Oceanogr. Res. Pap.* **167**, 103430 (2021).
51. Stranne, C., O'Regan, M., Jakobsson, M., Brüchert, V. & Ketzer, M. Can anaerobic oxidation of methane prevent seafloor gas escape in a warming climate? *Solid Earth* **10**, 1541–1554 (2019).
52. Luff, R., Wallmann, K. & Aloisi, G. Numerical modeling of carbonate crust formation at cold vent sites: significance for fluid and methane budgets and chemosynthetic biological communities. *Earth Planet. Sci. Lett.* **221**, 337–353 (2004).

**Publisher's note** Springer Nature remains neutral with regard to jurisdictional claims in published maps and institutional affiliations.

**Open Access** This article is licensed under a Creative Commons Attribution 4.0 International License, which permits use, sharing, adaptation, distribution and reproduction in any medium or format, as long as you give appropriate credit to the original author(s) and the source, provide a link to the Creative Commons licence, and indicate if changes were made. The images or other third party material in this article are included in the article's Creative Commons licence, unless indicated otherwise in a credit line to the material. If material is not included in the article's Creative Commons licence and your intended use is not permitted by statutory regulation or exceeds the permitted use, you will need to obtain permission directly from the copyright holder. To view a copy of this licence, visit <http://creativecommons.org/licenses/by/4.0/>.

© The Author(s) 2025



## Methods

### Study site

The continental shelf break 80 km west of the Lofoten Archipelago, offshore northern Norway, is characterized by a system of submarine canyons (Fig. 1). In two of these submarine canyons at ca. 800 m below sea level, the seafloor exhibits extensive SGD-related features including microbial mats, colonies of siboglinid worms and crusts of authigenic precipitates consisting of barite and Ca-carbonate<sup>17,28</sup> (Fig. 1). The freshened SGD is hypothesized to originate from Cenozoic-aged sedimentary rocks that have been incised by canyons forming bedrock exposures along the canyon walls<sup>28</sup> (Extended Data Fig. 1). The sedimentary rocks comprise alternating sandstone and mudstone strata with sandstones serving as groundwater conduits. Push cores were obtained from the bottom of both canyons (called 'Northern canyon' and 'Southern canyon') where recent sediments occur, covered by microbial mats ('BacMat') or worm tuff ('Worm'). Additionally, a set of cores named 'Background' were obtained upslope outside of the canyons, where the seafloor did not display any SGD-related features.

### Field sampling

The sediment cores were collected in late November 2021 during cruise P2107 on board R/V *G.O. Sars*. The push cores were collected using a remotely operated vehicle (ROV; *Ægir 6000*), allowing visual inspection of the seafloor. At all sample locations, multiple cores were obtained in parallel to accommodate the planned sub-sampling, including headspace gas sampling, porewater extraction and sediment slicing. Headspace gas sampling was performed immediately after core recovery through pre-drilled holes in the liners that were sealed off with tape during the dives. Sediment was collected in 20-ml glass headspace crimp vials (VWR, cat. no. 548-0055) that contained ~10 ml of Milli-Q water saturated in sodium chloride. The vials were sealed using Butyl injection stoppers and crimped aluminium caps (VWR, cat. no. 548-0058). After sampling, the headspace vials were stored at 4 °C until analysis. Porewater extraction was done through acid-washed Rhizon samplers (0.12–0.18 µm membrane pore size, Rhizosphere Research Products), and the porewater was collected in air-tight 20 ml polypropylene syringes (Henke-Ject). Materials used for porewater extraction and sample storage for cation analysis were acid-washed before use. During extraction, the cores were kept at 4 °C. When completed, the porewater was sub-sampled into different vials for the various planned analyses. For cation analysis, the porewaters were acidified with nitric acid (Suprapur, Sigma Aldrich). For stable and radioactive DIC carbon isotopic analyses and nutrient analysis, the porewater samples were kept frozen at –20 °C. All other vials were stored at 4 °C until further analysis. Total alkalinity was determined onboard using Gran titration, a potentiometric method whereby 0.01 M HCl (Suprapur, Sigmaaldrich) was used as titrant. After porewater extraction, the cores were sliced into separate fractions of 1 cm and the sediments were kept at 4 °C. Post-cruise, the sediments were freeze-dried and afterwards homogenized and pulverized before subsequent analyses.

### Radiocarbon analysis

The <sup>14</sup>C dating was performed with the MICADAS Accelerator Mass Spectrometry (AMS) at Atomki/Isotoptech Zrt in Debrecen, Hungary. The AMS procedure and preparation protocols for <sup>14</sup>C analysis of low-carbon samples are discussed in greater detail in previous work<sup>53–55</sup> but are briefly summarized here. For the TIC preparation, 5 ml of 85% phosphoric acid was added to 1 g of pre-dried sediment in an evacuated reaction vessel, which was subsequently stored in a heating block at 75 °C for 1 h. For the DIC analysis, the porewater was filtered through a 0.45-µm membrane and afterwards inserted into an evacuated reaction vessel sealed by a silicon septum. Similarly, 2 ml of phosphoric acid was added to the porewater, and the vessels were heated at 75 °C for 1 h. For POC analysis, the TIC fraction was removed first, after which the residual sediment was combusted. The TIC was

removed through the addition of 5 ml of 4% HCl to 1 g of sediment. The acid and sediments were well mixed and heated at 75 °C for 1 h. Afterwards, the acidic liquid was poured out and rinsed with Milli-Q to recover the mixture to a pH of 7. The samples were dried at 60 °C, and the dry sediment was, along with manganese dioxide, added to an ampule. The acid-insoluble fraction was combusted at 550 °C for a duration of 12 h. After the carbon was released in the form of CO<sub>2</sub>, the gas mixture was purified and concentrated using a preparation line that incorporated two cold traps. The first cold trap consisted out of a mixture of dry ice with isopropyl alcohol that trapped the water vapour at –75 °C, and the second cold trap used liquid nitrogen (–196 °C) to concentrate the CO<sub>2</sub>. For samples with >0.3 mgC, the CO<sub>2</sub> was collected into an ampule that contained 10 mg of Zn, 60 mg of TiH<sub>2</sub> and 4.5 mg of Fe. The graphitization process consisted of two combustion steps. First, the hydrogen was released by combusting the analyte for 3 h at 500 °C. Then, the graphitization reaction was initiated by heating the ampules with the reactants at 550 °C for 5 h. For lower carbon content between 0.3 and 0.1 mg, the TiH<sub>2</sub> was excluded and only the second combustion step at 550 °C was performed. Every sample was measured five times in total by using the AMS instrument during a single analysis cycle, with the reported s.d. representing the error ranges of these reiterations. During the analysis, control standards (OxII) and calibration standards were included. The data were processed and exported using the BATS software<sup>56</sup> and are reported in pMC<sup>57</sup>.

### Stable isotope analyses

The stable carbon and oxygen isotope analyses of TIC, DIC and methane were performed in the stable isotope laboratory at Stockholm University on a Gasbench-MAT253 (Thermo Scientific) for the TIC and DIC, and on a Trace Gas Ultra/GC Isolink (Thermo Scientific) for methane. For the TIC and DIC, both international (NBS18/ NBS19/ IAEA-603) and inhouse control standards were included, and for CH<sub>4</sub>, a standard gas was included to ensure instrument performance. Presented error ranges represent the s.d. of these standards, which were <0.04‰ for δ<sup>13</sup>C<sub>DIC</sub>, <0.14‰ for δ<sup>13</sup>C<sub>TIC</sub>, <0.22‰ for δ<sup>18</sup>O<sub>TIC</sub> and <0.05‰ for δ<sup>13</sup>C<sub>CH<sub>4</sub></sub>. The POC weight percentage and δ<sup>13</sup>C values were measured by elemental analyser isotope ratio mass spectrometry at Iso-Analytical in Crewe, UK with δ<sup>13</sup>C<sub>POC</sub> having a s.d. of <0.17‰. All δ<sup>13</sup>C values are reported against Vienna Pee Dee Belemnite (VPDB), following the international standard delta signature notation<sup>57</sup>. The porewater was analysed for δ<sup>2</sup>H and δ<sup>18</sup>O using the Liquid Water Isotope Analyzer (L2140-i, Picarro) at Stockholm University. The delta notations are reported relative to Vienna Standard Mean Ocean Water (VSMOW)<sup>57</sup>.

### Porewater ion analyses

The chlorinity was determined using a potentiometric titration with silver nitrate as precipitant and EDTA as mediator<sup>58</sup>. Before titration, the solution was brought to a pH between 10 and 11 by adding HNO<sub>3</sub> and NaOH, respectively. To calculate the equivalent point, the intersect of the two tangent linear titration curves was determined. International Association for the Physical Sciences of the Oceans Standard Seawater was deployed as a control standard to ensure the quality of the chemicals and titration set-up. The standard replicates were used to calculate the error range (1σ)<sup>57</sup>. Sulfate concentrations were measured at Stockholm University with ion chromatography (IC20, Dionex), where the samples were diluted by a factor of 50 before measurement. Uncertainty ranges were calculated from the included standards<sup>57</sup>. The cation concentrations were analysed by inductively coupled plasma–atomic emission spectroscopy at Stockholm University (iCAP 6500, Thermo Fisher). The samples were diluted 1,000 times for the measurement of major cations (Ca, K, Mg, Na and S) and 100 times for trace cations (B, Ba, Li, Mn and Si). The reported cation concentrations have the following uncertainties: ≤3% for calcium (Ca), ≤4% for potassium (K), ≤4% for magnesium (Mg), ≤1% for sodium (Na), ≤4% for sulfur (S), ≤2% for boron (B), ≤3% for barium (Ba), ≤1% for lithium (Li), ≤5% for manganese

(Mn) and  $\leq 3\%$  for silicon (Si)<sup>57</sup>. These uncertainties were calculated by taking the average s.d. of two duplicate International Association for the Physical Sciences of the Oceans Standard Seawater measurements and three duplicate sample measurements.

### Methane concentrations

Methane concentrations were calculated from porosity and gas chromatography (GC) measurements. Before GC analysis, the headspace gas vials were stirred on a shaker for 45 min to force all gasses into the headspace. Gas (50  $\mu\text{l}$ ) was extracted from the headspace with a syringe and injected directly onto a column that connects to a flame ionization detector of the GC (SRI, 8610 C). A two-point calibration curve was constructed from standard reference gasses. To determine the porosity, subsets of sediment samples were weighted before and after drying at 60 °C for several days. To correct for precipitated salt, a fixed salinity of 0.035 g  $\text{ml}^{-1}$  was assumed. A porewater density of 1.024 g  $\text{ml}^{-1}$  was applied to convert the weight difference into pore volume. The obtained porosity (uncertainty  $<0.1$ ) and gas mole fractions (relative standard deviation  $<9.7\%$ ) were finally combined to calculate  $\text{CH}_4$  gas concentrations per volume of porewater (that is, molar concentration of methane)<sup>57</sup>. Owing to potential degassing during the dive and sampling, we acknowledge that actual methane concentrations are probably higher.

### Barite content

Barite abundances in two sediment cores were determined at Tartu University, Estonia by X-ray diffraction analysis from unoriented preparations on a Bruker D8 Advance diffractometer using Cu K $\alpha$  radiation and a LynxEye positive sensitive detector in the  $2\theta$  range of 2–70°. Abundances were interpreted and modelled using the Rietveld algorithm-based program Topaz. The relative error of quantification is better than 10%.

### Three end-member mixing model

To determine the saline and fresh submarine groundwater (sSG and fSG, respectively) contributions, a conventional two end-member mixing model was used<sup>59</sup>

$$\text{Cl}_{\text{pw}} = f_{\text{sSG}} \text{Cl}_{\text{sSG}} + (1 - f_{\text{sSG}}) \text{Cl}_{\text{fSG}}, \quad (1)$$

with  $\text{Cl}_{\text{sSG}}$  presumed to be 560 mM,  $\text{Cl}_{\text{fSG}}$  to be 0 mM,  $f_{\text{sSG}}$  being the fraction of sSG and  $\text{Cl}_{\text{pw}}$  being the measured dissolved chloride concentration of sampled porewater.  $f_{\text{sSG}}$  can thus be constrained. A three end-member mixing model<sup>59</sup> was employed to partition the  $^{14}\text{C}$  activity into distinct end-members

$$C_{\text{pw}} A_{\text{pw}}(t) = C_{0,\text{sSG}} f_{\text{sSG}} A_{\text{sSG}}(t) + C_{0,\text{fSG}} (1 - f_{\text{sSG}}) A_{\text{fSG}}(t) + C_{\text{chem}} A_{\text{chem}}(t) \quad (2)$$

where  $A_{\text{fSG}}(t)$  and  $A_{\text{sSG}}(t)$  are the end-member  $^{14}\text{C}$  activities of fSG and sSG, respectively, at the time of sampling<sup>60</sup>.  $A_{\text{pw}}(t)$  is the activity for bulk DIC in our porewater samples also at present time  $t$ . The activity  $A_{\text{chem}}(t)$  represents the addition of continental margin material introduced through biogeochemical reactions or carbonate dissolution and was assumed to be fully depleted in radiocarbon (that is,  $A_{\text{chem}}(t) = 0$ ) given the ancient rocks along the flow path (Extended Data Fig. 1). The term  $C_{\text{chem}} A_{\text{chem}}(t)$  in equation (2) can thus be dropped entirely. The DIC porewater concentration,  $C_{\text{pw}}$ , was estimated by subtracting hydrogen sulfide concentrations<sup>17</sup> from total alkalinity. For PC29,  $C_{\text{pw}}$  was estimated at approximately 4,000  $\mu\text{M}$ , while higher alkalinities in PC37 yield a  $C_{\text{pw}}$  of around 4,500  $\mu\text{M}$ . The DIC concentration of Subarctic Intermediate Water ( $C_{0,\text{sSG}}$ ) was estimated to be 2,100  $\mu\text{M}$  (ref. 61). Subglacial water primarily originates from supraglacial meltwater<sup>41,62</sup>, and upon entering the groundwater system, it carries the DIC sourced from the atmosphere. Dissolved  $\text{CO}_2$  levels in subglacial waters can, on

average, be assumed to be in atmospheric equilibrium<sup>39</sup>. To determine the past dissolved  $\text{CO}_2$  in subglacial waters ( $C_{0,\text{fSG}}$ ), Henry's law and the van't Hoff equation were applied<sup>63</sup>

$$C_{\text{CO}_2} = K_{\text{H}} P_{\text{CO}_2} \quad (3)$$

$$K_{\text{H}}(T_{273.15}) = K_{\text{H}}(T_{298.15}) \exp\left(-\frac{\Delta H_{\text{sol}}}{R} \left(\frac{1}{T_2} - \frac{1}{T_1}\right)\right). \quad (4)$$

Assuming an average temperature of 0 °C (273.15 K), the Henry's law constant ( $K_{\text{H}}$ ) was calculated to be  $3.165 \times 10^{-2} \text{ mol}^{-1} \text{ l atm}$  (ref. 63). During the Bølling–Allerød and Younger Dryas periods, atmospheric  $\text{CO}_2$  levels were around 240 ppm (ref. 64), resulting in a  $p\text{CO}_2$  of  $2.4 \times 10^{-4} \text{ atm}$ . This results in a  $C_{0,\text{fSG}}$  of 7.6  $\mu\text{mol l}^{-1}$ .

Owing to  $^{14}\text{C}$  decay, the activities of fSG, sSG and bulk porewater are time dependent.  $A_{\text{fSG}}(t)$  and  $A_{\text{sSG}}(t)$  were calculated according to<sup>60</sup>

$$A_{\text{fSG}}(t) = A_{\text{fSG}}(t_0) e^{-\lambda_1(t-t_0)_{\text{fSG}}}, \quad (5)$$

$$A_{\text{sSG}}(t) = A_{\text{sSG}}(t_0) e^{-\lambda_1(t-t_0)_{\text{sSG}}}, \quad (6)$$

where  $A(t_0)$  is the initial  $^{14}\text{C}$  activity after recharge, assumed to be 80 pMC ( $= A_{\text{fSG}}(t_0)$ ) on the basis of average subglacial water  $^{14}\text{C}$  activities<sup>40</sup>, and 98 pMC ( $= A_{\text{sSG}}(t_0)$ ) for the seawater component, deduced from present bottom water  $^{14}\text{C}$  contents (Fig. 2).  $\lambda_1$  is the Libby decay constant ( $\lambda_1 = 1/8,033 \text{ yr}^{-1}$ )<sup>60</sup>. The residence time of sSG ( $(t - t_0)_{\text{sSG}}$ ) is the primary target of this calculation, with the residence time of fSG ( $(t - t_0)_{\text{fSG}}$ ) and  $A_{\text{sSG}}(t)$  being unknowns at this point.

With this aim, we substituted  $A_{\text{fSG}}(t)$  into equation (2) with equation (5)

$$C_{\text{pw}} A_{\text{pw}}(t) = C_{0,\text{sSG}} f_{\text{sSG}} A_{\text{sSG}}(t) + C_{0,\text{fSG}} (1 - f_{\text{sSG}}) (A_{\text{fSG}}(t_0) e^{-\lambda_1(t-t_0)_{\text{fSG}}}), \quad (7)$$

which can be rewritten as

$$A_{\text{sSG}}(t) = \frac{1}{C_{0,\text{sSG}} f_{\text{sSG}}} (C_{\text{pw}} A_{\text{pw}}(t) - C_{0,\text{fSG}} (1 - f_{\text{sSG}}) (A_{\text{fSG}}(t_0) e^{-\lambda_1(t-t_0)_{\text{fSG}}}). \quad (8)$$

$A_{\text{sSG}}(t)$  can thus be solved by assuming  $(t - t_0)_{\text{fSG}}$  to be between 14 and 32 ka (refs. 42,44,45) (Fig. 1c) and by deriving  $f_{\text{sSG}}$  from the measured porewater chloride concentration (equation (1)).

Then,  $(t - t_0)_{\text{sSG}}$  was solved for by rearranging equation (6) as

$$(t - t_0)_{\text{sSG}} = -8,033 \ln \left( \frac{A_{\text{sSG}}(t)}{A_{\text{sSG}}(t_0)} \right). \quad (9)$$

We plotted  $(t - t_0)_{\text{sSG}}$  against the measured dissolved chloride concentration with different  $A_{\text{fSG}}(t)$  indicated in Fig. 4a ref. 57.

### Reaction–transport model

A one-dimensional reaction–transport model<sup>50,65</sup> using mass balance calculations of  $^{12}\text{C}$  and  $^{13}\text{C}$  was extended for this study to include the  $^{14}\text{C}$  isotopologue<sup>66</sup>. The solute transport equation is numerically solved using the Crank–Nicholson scheme. Solute diffusion was modelled using Fick's law, with diffusion constants (Supplementary Table 1) taken from ref. 67. The diffusion coefficients are calculated according to

$$D_{\text{solute}} = \frac{D_{\text{constant}}}{1 - \ln(\phi^2)}, \quad (10)$$

where  $\phi$  represents the porosity. The burial velocity, determined from shell ages, was set to 0.000059  $\text{m yr}^{-1}$ , which is negligible relative to advection velocities. Given the low groundwater flow velocities,

mechanical dispersion was also considered negligible. To minimize the influence of bioturbation, porewater profiles from a bacterial mat habitat (PC29) were used for model fitting.

The model considers nine solute species ( $^{12}\text{DIC}$ ,  $^{13}\text{DIC}$ ,  $^{14}\text{DIC}$ ,  $^{12}\text{CH}_4$ ,  $^{13}\text{CH}_4$ ,  $^{14}\text{CH}_4$ ,  $\text{Ca}$ ,  $\text{NH}_4$  and  $\text{SO}_4$ ) and six solid phases ( $^{12}\text{TIC}$ ,  $^{13}\text{TIC}$ ,  $^{14}\text{TIC}$ ,  $^{12}\text{POC}$ ,  $^{13}\text{POC}$  and  $^{14}\text{POC}$ ) and accounts for the following six major carbon reaction pathways:

- AOM coupled to sulfate reduction
- Back flux reaction of AOM
- $\text{CO}_2$  reduction
- Biomass accumulation by anaerobic methanotropic archaea
- POC degradation through sulfate reduction and fermentation
- Authigenic carbonate precipitation

The isotopic fractionation factors ( $\alpha_{13}$ ) applied for each of the six reactions can be found in Supplementary Table 2. The  $^{14}\text{C}/^{12}\text{C}$  fractionation factor ( $\alpha_{14}$ ) is directly calculated from the  $^{13}\text{C}/^{12}\text{C}$  fractionation using

$$\alpha_{14} = \alpha_{13}^b, \quad (11)$$

where  $\alpha$  is the fractionation factor of the corresponding isotopologue and  $b$  is the relative shift  $\Delta R/R$  (with  $R$  being the ratio of heavy isotope to light isotope) from  $^{14}\text{C}/^{12}\text{C}$  to  $^{13}\text{C}/^{12}\text{C}$ . Temperature-dependent values of  $b$  have been reported to range between  $b_{\min} = 1.84$  at 20 K and  $b_{\max} = 1.98$  at 2,000 K (ref. 68). In the model experiments,  $b$  was set to 1.9. To account for radioactive decay, a fraction of the  $^{14}\text{C}$  was removed from every carbon pool after every time iteration according to

$$A = A_0 e^{-\lambda_c t}, \quad (12)$$

where  $\lambda_c$  is the Cambridge decay constant, equal to  $8.267^{-1} \text{ yr}^{-1}$  (ref. 60). The upper solute boundary conditions (Supplementary Table 3) were used as initial conditions, whereafter the model was run until equilibrium was reached. Bottom solute boundary conditions can be found in Supplementary Table 4.

A downcore porosity profile was constructed according to

$$\phi = \phi_{\text{bottom}} + (\phi_{\text{surface}} - \phi_{\text{bottom}}) e^{-\lambda z}, \quad (13)$$

where  $\lambda$  controls the downcore decrease of the porosity (set to  $-22 \text{ m bulk space}^{-1}$ ),  $z$  is the core depth,  $\phi_{\text{surface}}$  is the porosity at the surface of the core (set to  $0.52 \text{ m}^3 \text{ pore space per m}^3 \text{ bulk space}$ ) and  $\phi_{\text{bottom}}$  is that at the bottom (set to  $0.33 \text{ m}^3 \text{ pore space per m}^3 \text{ bulk space}$ ). These values were fitted to measured porosity data.

For the first modelling experiment (Extended Data Fig. 2), the reaction–transport model was, to the best ability possible, fitted to the observations. Firstly, POC degradation was constrained using the  $\text{NH}_4^+$  concentrations. Then, using the profile shapes, alkalinity measurements and isotopic signatures, the remaining reactions and advection velocity were fitted. It was not possible to fit both the  $\delta^{13}\text{C}_{\text{DIC}}$  and the alkalinity without bringing the AOM fractionation below 1.0. Nevertheless, it is very likely that AOM rates are extremely high owing to the high in situ alkalinity production. Additional numerical simulations with the upwards advection set to 0 or the AOM rate set to 0 were performed to assess the importance of these two processes for the studied SGD site (Extended Data Fig. 2). For the second numerical experiment (Extended Data Fig. 7), bottom boundary conditions of  $^{14}\text{C}_{\text{CH}_4}$  were varied between fully radiocarbon depleted, to 35 and 71 pMC, with the latter being the radiocarbon content of the in situ POC. For the third numerical experiment (Extended Data Fig. 9), the upwards advection velocity was increased to  $0.5 \text{ m yr}^{-1}$  and  $3.0 \text{ m yr}^{-1}$  to assess the extent to which the SMTZ would shift towards the sediment–water interface. No higher advection velocities were applied because of numerical instability considerations.

## Data availability

All geochemical analyses data, radiocarbon calculations, source data for Figs. 1c, 2, 3 and 4a and Extended Data Figs. 3, 4–6, 8 and 10 are publicly available via the Bolin Centre Database at <https://doi.org/10.17043/ten-hietbrink-2025-marine-geochemistry-1>. The Lista Meteoric Water Line data are available via the GNIP Database at <https://nucleus.iaea.org/wiser>. An overview of the push core sample sites is included in the Supplementary Information.

## Code availability

The MATLAB reaction–transport model and Python codes used for data plotting are available via the Bolin Centre git at <https://doi.org/10.57669/ten-hietbrink-2025-marine-geochemistry-1.0.0>.

## References

- Molnár, M. et al. C-14 analysis of groundwater down to the millilitre level. *Nucl. Instrum. Methods Phys. Res. B* **294**, 573–576 (2013).
- Molnár, M. et al. Status report of the new AMS  $^{14}\text{C}$  sample preparation lab of the Hertelendi Laboratory of Environmental Studies (Debrecen, Hungary). *Radiocarbon* **55**, 665–676 (2013).
- Molnár, M. et al. EnvironMICADAS: a mini  $^{14}\text{C}$  AMS with enhanced gas ion source interface in the Hertelendi Laboratory of Environmental Studies (HEKAL), Hungary. *Radiocarbon* **55**, 338–344 (2013).
- Wacker, L., Christl, M. & Sýnal, H. A. Bats: a new tool for AMS data reduction. *Nucl. Instrum. Methods Phys. Res. B* **268**, 976–979 (2010).
- ten Hietbrink, S. et al. Marine sediments and porewater geochemical data for a submarine groundwater discharge site offshore northern Norway. Dataset version 1. *Bolin Centre Database* <https://doi.org/10.17043/ten-hietbrink-2025-marine-geochemistry-1> (2025).
- Hong, T. K., Kim, M. H. & Czae, M. Z. Determination of chlorinity of water without the use of chromate indicator. *Int. J. Anal. Chem.* **1**, 602939 (2010).
- Kirchner, J. W. Mixing models with multiple, overlapping, or incomplete end-members, quantified using time series of a single tracer. *Geophys. Res. Lett.* **50**, e2023GL104147 (2023).
- Stenström, K., Skog, G., Georgiadou, E., Genberg, J. & Mellström, A. A guide to radiocarbon units and calculations, LUNFD6(NFFR-3111)/1-17/(2011) (Nuclear Physics, Lund University, 2011).
- Feely, R. A., Sabine, C. L., Takahashi, T. & Wanninkhof, R. Uptake and storage of carbon dioxide in the ocean: the global  $\text{CO}_2$  survey. *Oceanography* **14**, 18–32 (2001).
- Chu, W. et al. Extensive winter subglacial water storage beneath the Greenland Ice Sheet. *Geophys. Res. Lett.* **43**, 12–484 (2016).
- Sander, R. Compilation of Henry's law constants (version 5.0. 0) for water as solvent. *Atmos. Chem. Phys.* **23**, 10901–12440 (2023).
- Ahn, J. et al. A record of atmospheric  $\text{CO}_2$  during the last 40,000 years from the Siple Dome, Antarctica ice core. *J. Geophys. Res. Atmos.* **109**, D13305 (2004).
- Hong, W. L., Torres, M. E., Kim, J. H., Choi, J. & Bahk, J. J. Towards quantifying the reaction network around the sulfate–methane-transition-zone in the Ulleung Basin, East Sea, with a kinetic modeling approach. *Geochim. Cosmochim. Acta* **140**, 127–141 (2014).
- ten Hietbrink, S. & Hong, W.-L. Reaction–transport model and data plotting code for a submarine groundwater discharge site offshore northern Norway, software version 1.0.0. *Bolin Centre Code Repository* <https://doi.org/10.57669/ten-hietbrink-2025-marine-geochemistry-1.0.0> (2025).
- Boudreau, B. P. *Diagenetic Models and Their Implementation* Vol. 505, p. 132 (Springer, 1997).

68. Fahrni, S. M. et al. Reassessment of the  $^{13}\text{C}/^{12}\text{C}$  and  $^{14}\text{C}/^{12}\text{C}$  isotopic fractionation ratio and its impact on high-precision radiocarbon dating. *Geochim. Cosmochim. Acta* **213**, 330–345 (2017).
69. Tasrianto, R. & Escalona, A. Rift architecture of the Lofoten–Vesterålen margin, offshore Norway. *Mar. Pet. Geol.* **64**, 1–16 (2015).
70. Meza-Cala, J. C., Tsikalas, F., Faleide, J. I. & Abdelmalak, M. M. New insights into the late Mesozoic–Cenozoic tectono-stratigraphic evolution of the northern Lofoten–Vesterålen margin, offshore Norway. *Mar. Pet. Geol.* **134**, 105370 (2021).

## Acknowledgements

This research has received funding from the Norwegian Financial Mechanism 2014–2021 nr 2019/34/H/ST10/00645 (W.-L.H., B.S., A.L., A.S., J.K. and S.t.H.). It additionally has received funding from the European Union's Horizon 2020 research and innovation programme under grant agreement no. 871149 (W.-L.H.), the Swedish Research Council (VR) under the project 'Cyrosphere-driven submarine groundwater discharge in the Arctic' (project no. 2021-04962) (W.-L.H.) and the Swedish Foundation for International Cooperation in Research and Higher Education under project IB2022-9230 (W.-L.H. and B.D.). Sampling from the Japan/East Sea was supported by the National Research Foundation of Korea (NRF-2023K2A9A2A12000309) (J.-H.K.). The contribution of J.K. to this research was supported by the Research Council of Norway (grant no. 332635) and the European Union through ERC grant no. 101118519. We thank the crew of R/V G.O. Sars, T.-H. Huang and E. Ståhl for their contributions to the sampling campaign. Furthermore, we thank J. Steinbach, H. Yao, K. Hajnal, T. Bisander and the Hekal Laboratory in Debrecen, Hungary for all their support performing the geochemical analyses.

## Author contributions

S.t.H. carried out data interpretation and wrote the study with contributions from all authors. W.-L.H. devised the project, with

funding acquired by W.-L.H., B.S., A.S., A.L. and J.-H.K. Fieldwork and sampling were done by W.-L.H., J.K., A.L., B.S., A.S. and J.-H.K. Data analysis was done by S.t.H., W.-L.H., B.S. and A.L. The ice sheet data were compiled by H.P. Reaction–transport modelling was performed by S.t.H. and W.-L.H. The hydrogeological modelling was done by S.t.H., supervised by B.D. All authors reviewed and contributed to the paper.

## Funding

Open access funding provided by Stockholm University.

## Competing interests

The authors declare no competing interests.

## Additional information

**Extended data** is available for this paper at <https://doi.org/10.1038/s41561-025-01750-z>.

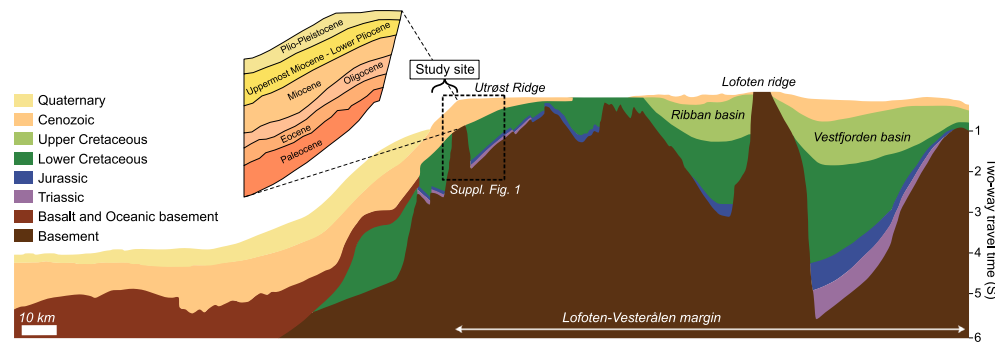
**Supplementary information** The online version contains supplementary material available at <https://doi.org/10.1038/s41561-025-01750-z>.

**Correspondence and requests for materials** should be addressed to S. ten Hietbrink or W.-L. Hong.

**Peer review information** *Nature Geoscience* thanks Christian Berndt and Boris van Breukelen for their contribution to the peer review of this work. Primary Handling Editors: Alireza Bahadori and James Super, in collaboration with the *Nature Geoscience* team.

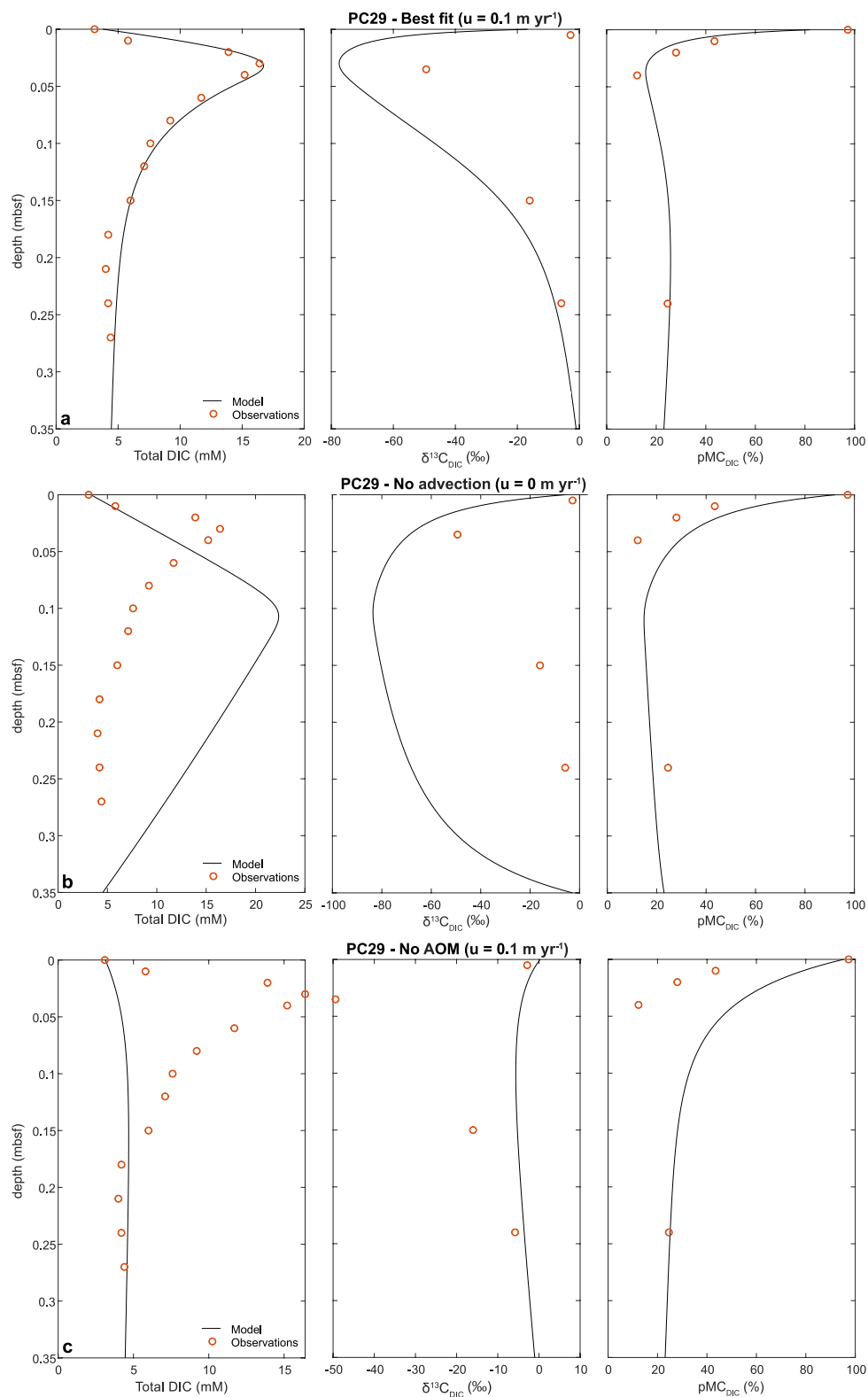
**Reprints and permissions information** is available at [www.nature.com/reprints](http://www.nature.com/reprints).



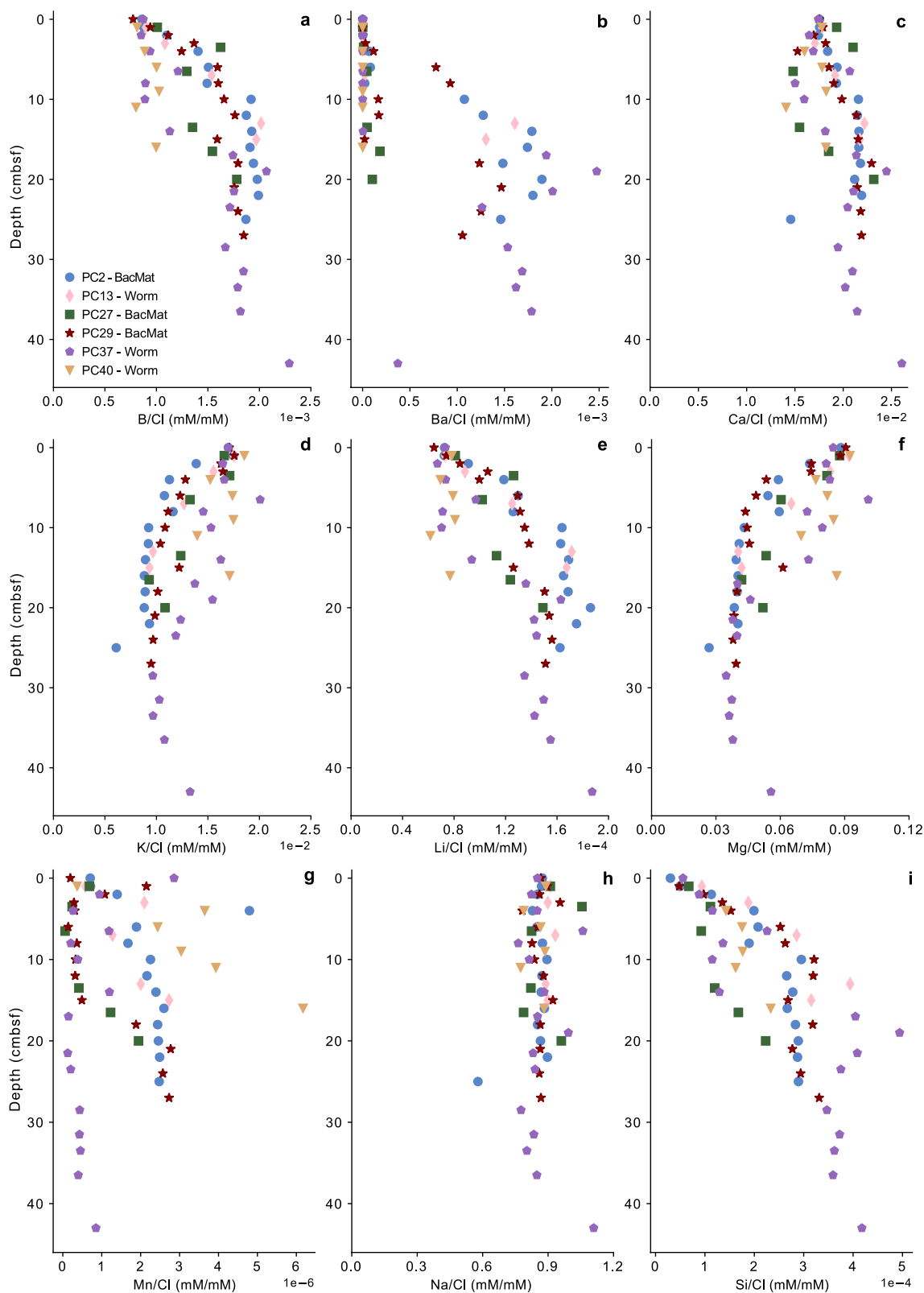


**Extended Data Fig. 1 | Stratigraphy of the Lofoten-Vesterålen margin.** The figure was adapted from Tasrianto et al. (2015)<sup>69</sup> and Meza-Cala et al. (2021)<sup>70</sup>. The Cenozoic strata, composed of clays, sandstones and conglomerates<sup>69</sup>, outcrop within the submarine canyons near the shelf break and are proposed as hosts for discharging groundwater<sup>28</sup>. The Top Cenozoic sequence is dominated by mud<sup>69</sup>

(based on data from well 6710/10-1), with the Plio-Pleistocene sequence being composed of glacio-marine sedimentary successions<sup>70</sup>. The black dotted box indicates the area magnified in the Supplementary Information Fig. 1. Figure adapted with permission from ref. 69, Elsevier.



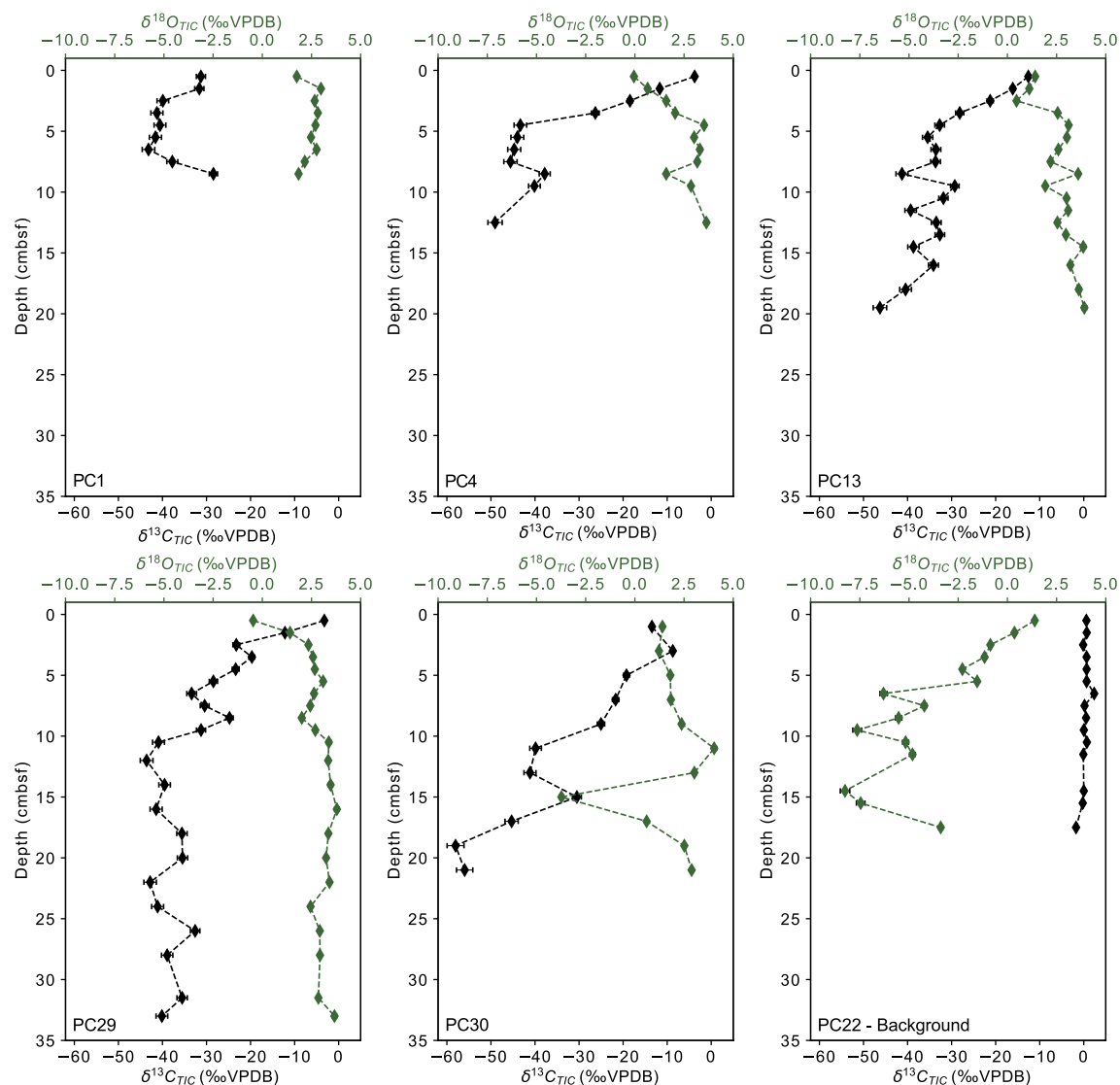
**Extended Data Fig. 2 | Best fit of the reaction-transport model.** (a) The best fit was found for an upward advection velocity of  $0.1 \text{ m yr}^{-1}$  and high AOM rates. The importance of these two processes for the DIC profiles at this site is illustrated by an experiment with no advection (b) and an experiment with no AOM (c).



**Extended Data Fig. 3 | Cation concentrations normalized against chlorinity.** Porewater cation concentrations of Boron (a), Barium (b), Calcium (c), Potassium (d), Lithium (e), Magnesium (f), Manganese (g), Sodium (h) and Silicon (i).

The reported cation concentrations have the following uncertainties: calcium

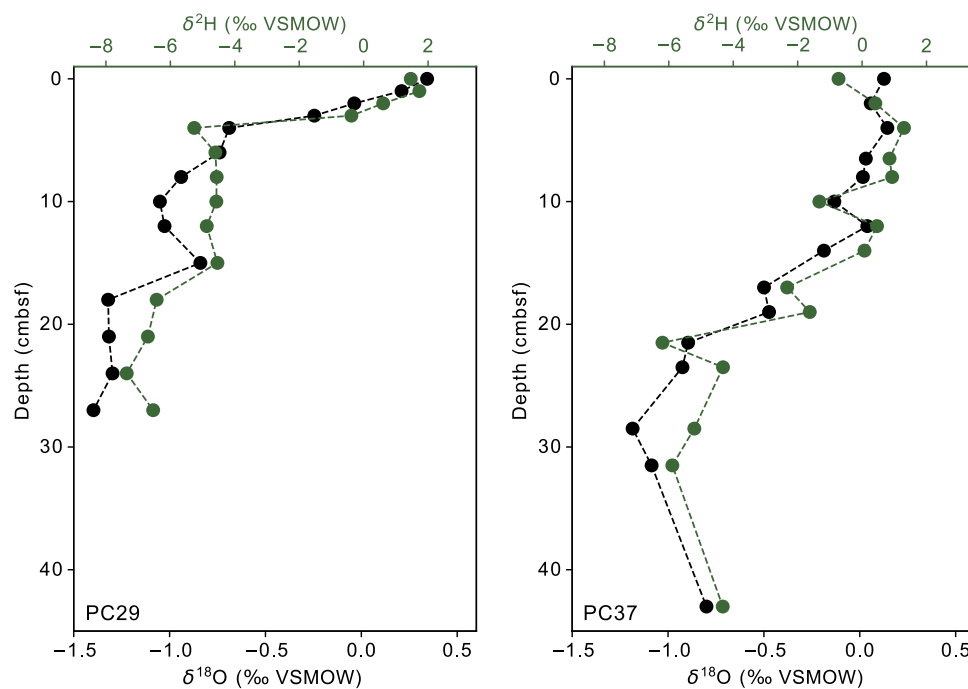
(Ca)  $\leq 3\%$ , potassium (K)  $\leq 4\%$ , magnesium (Mg)  $\leq 4\%$ , sodium (Na)  $\leq 1\%$ , sulfur (S)  $\leq 4\%$ , boron (B)  $\leq 2\%$ , barium (Ba)  $\leq 3\%$ , lithium (Li)  $\leq 1\%$ , manganese (Mn)  $\leq 5\%$  and silicon (Si)  $\leq 3\%$ .



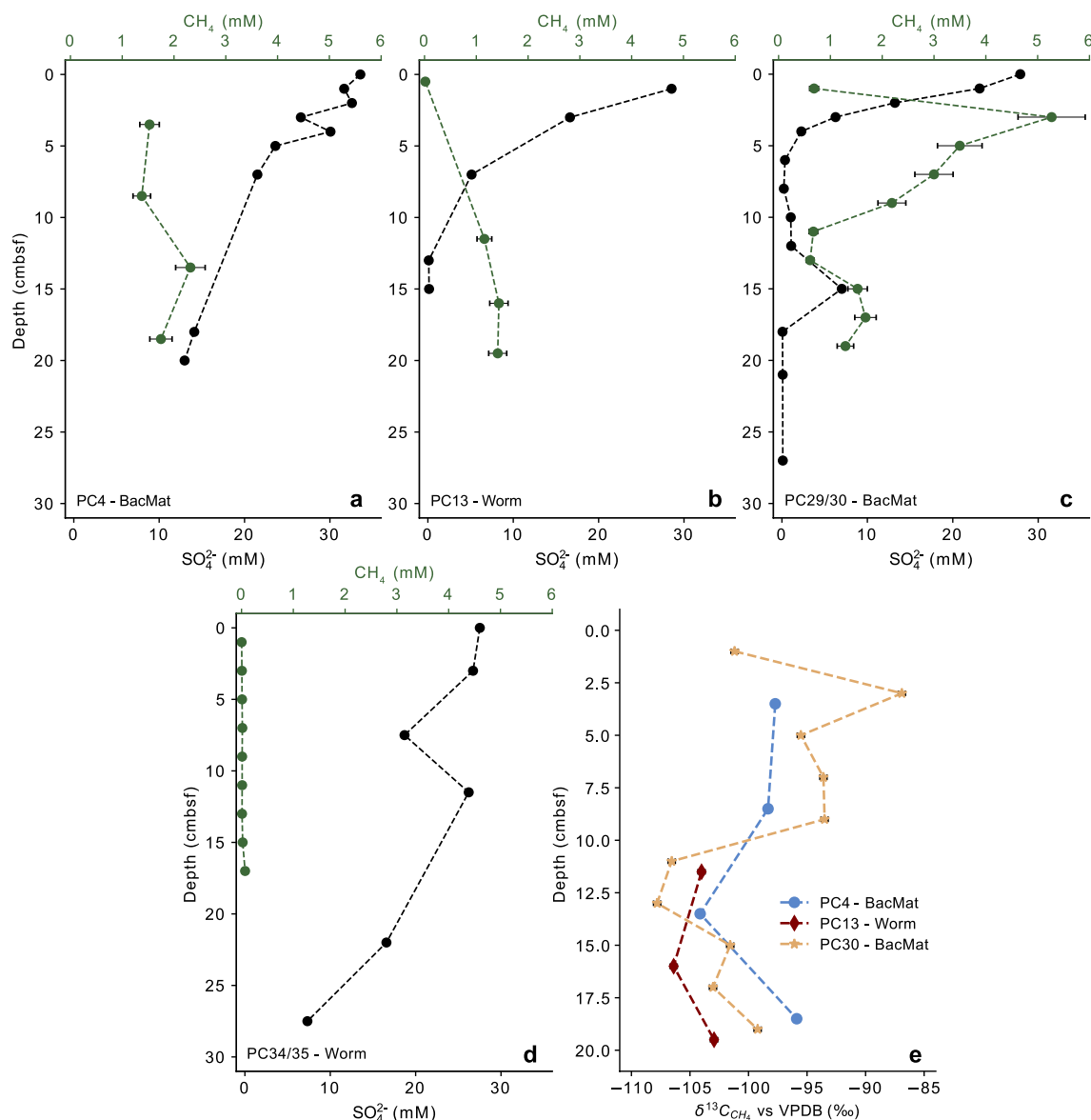
**Extended Data Fig. 4 |  $\delta^{13}\text{C}$  and  $\delta^{18}\text{O}$  signatures of the Total Inorganic Carbon sediment fraction.** The TIC isotopic signatures are dominated by authigenic carbonate that is depleted in  $^{13}\text{C}$  and enriched in  $^{18}\text{O}$  and shows a stark contrast

with the background core (PC22) that is unaffected by microbial seafloor activity. The error bars indicate the mean percent error calculated from all standards ( $n = 45$ ).



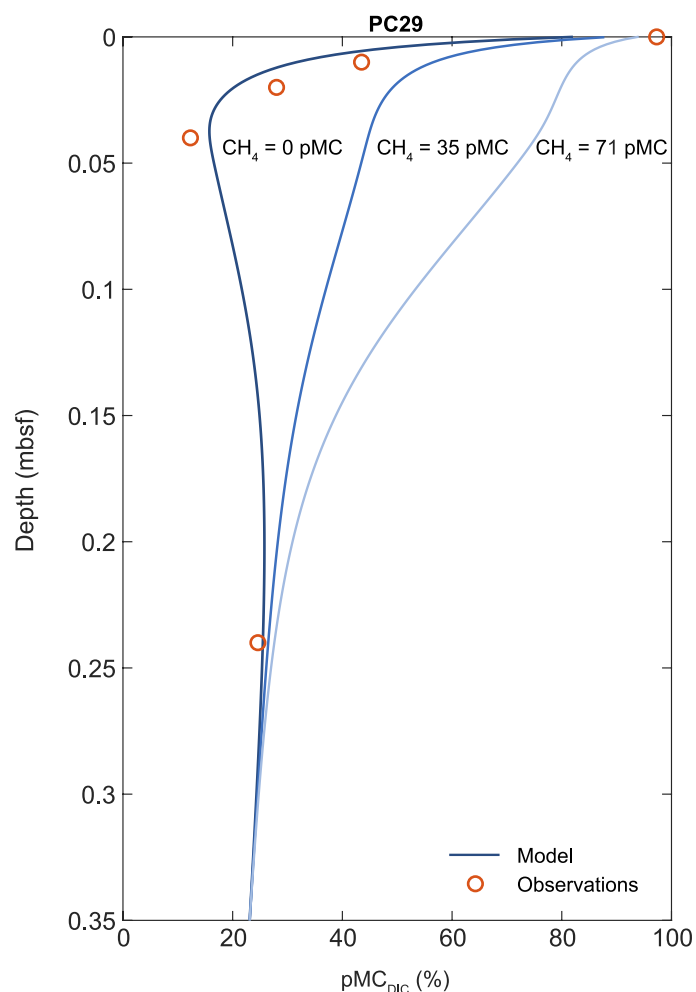


**Extended Data Fig. 5 | Downcore profiles of the  $\delta^{18}\text{O}_{\text{H}_2\text{O}}$  and  $\delta^2\text{H}_{\text{H}_2\text{O}}$  signatures for PC29 and PC37.  $\delta^{18}\text{O}$  and  $\delta^2\text{H}$  values are higher at the top of the core due to mixing with seawater.**



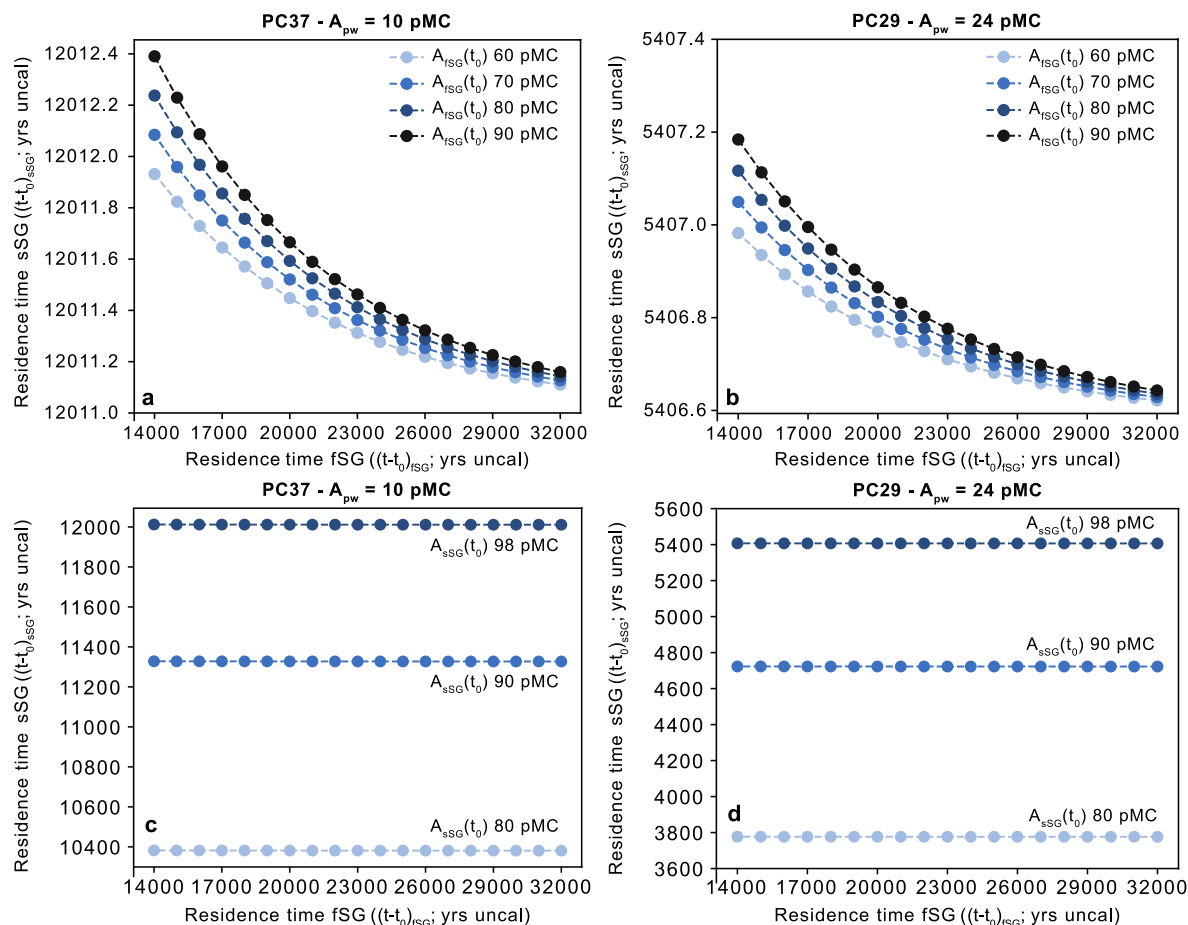
**Extended Data Fig. 6 | Porewater methane-sulfate concentrations and methane  $\delta^{13}\text{C}$  signatures.** Methane and sulfate profiles indicate the presence of sulfate-methane transition zones (b and c), or indicate that the SMTZ is situated deeper in the sediments (a and d). Low  $\delta^{13}\text{C}_{\text{CH}_4}$  signatures suggest a biogenic origin of the methane (e). Degassing of CH<sub>4</sub> during core recovery cannot be

ruled out, hence actual CH<sub>4</sub> concentrations are likely higher. The error bars in (a–d) represent the combined percent error range resulting from porosity uncertainties and the standard deviation of the 1% CH<sub>4</sub> standard (n = 4). The error bars in (e) represent the standard deviation derived from the reference gas (n = 8).



**Extended Data Fig. 7 | Best fit scenario with different CH<sub>4</sub> <sup>14</sup>C bottom boundary conditions.** To match the observed offset towards more <sup>14</sup>C-depleted DIC, near radiocarbon-free methane is required. The 71 pMC is the in-situ <sup>14</sup>C content of

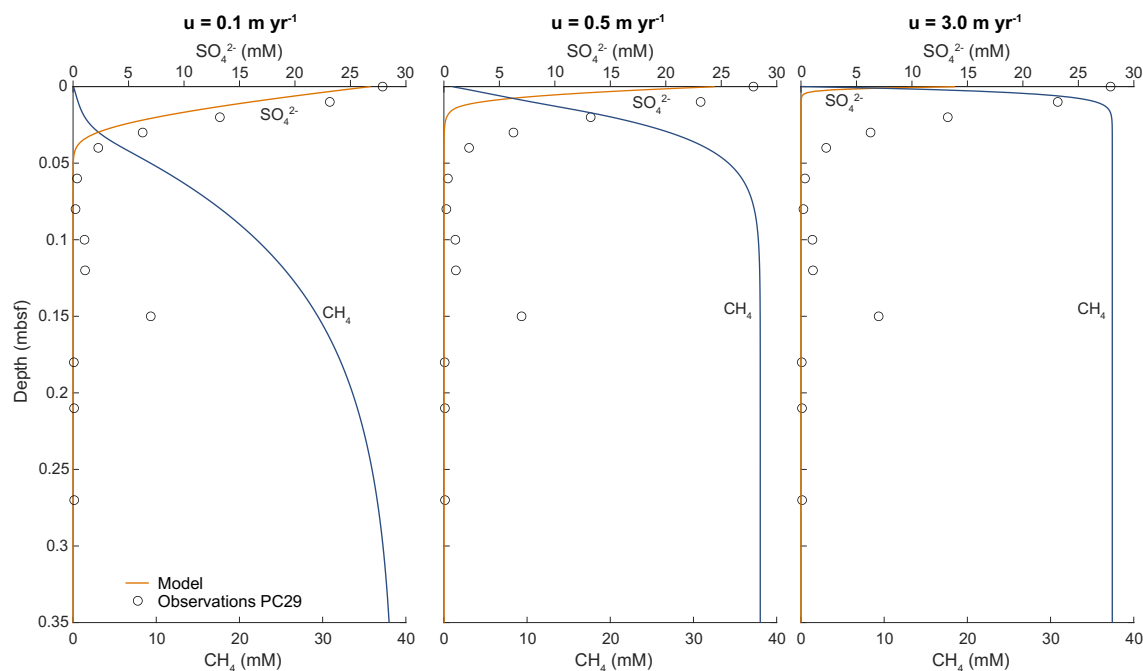
the POC and therefore the highest possible methane <sup>14</sup>C content. These model experiments support that the methane must have a near radiocarbon-free precursor and therefore likely originates from much deeper in the sediments.



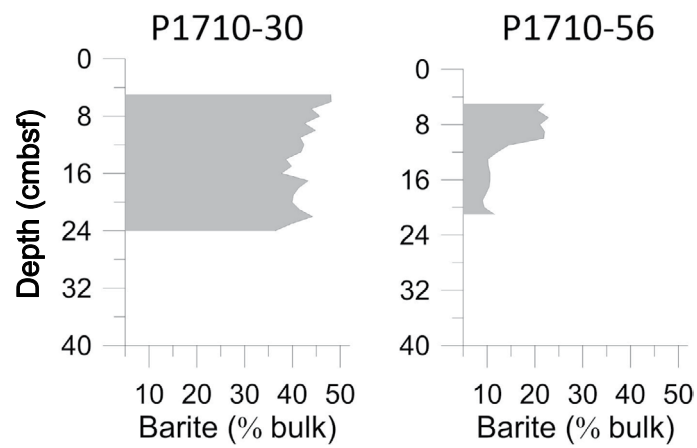
**Extended Data Fig. 8 | Sensitivity analysis of the initial  $^{14}\text{C}$  activity of the saline submarine groundwater ( $A_{SSG}(t_0)$ ) and fresh submarine groundwater ( $A_{FSG}(t_0)$ ) components.** As the porewaters are predominantly comprised of seawater, the initial  $^{14}\text{C}$  activity assumption of sSG has a greater impact on the calculated sSG residence time (c-d) compared to that of a varying initial  $^{14}\text{C}$  activity of fSG

(a-b). The  $A_{FSG}(t_0)$  assumption introduces an uncertainty in the order of 0.5 years at most. That of  $A_{SSG}(t_0)$  could introduce a maximum uncertainty of 1,600 years provided  $A_{SSG}(t_0)$  equals 80 pMC, which is considered unlikely due to the relatively high  $^{14}\text{C}$  content of seawater (Fig. 2).





**Extended Data Fig. 9 | Sulfate-methane profiles for different upward advection velocities of discharged groundwater.** Increased hydraulic head gradients and subsequent increased groundwater advection velocities ( $u$ ) as a result of glacial loading have the potential to move the SMTZ up to the sediment-water interface, resulting in the precipitation of barite on the seafloor.



**Extended Data Fig. 10 | High barite content in the sediment cores at the LV site.** Barite concentrations in two push cores collected during the NGU 1710 cruise in 2017 from the same submarine canyons show high levels of barite within the marine sediments.